Distributed Optimization for Reactive Power Sharing and Stability of Inverter-Based Resources Under Voltage Limits

Babak Abdolmaleki, *Graduate Student Member, IEEE*, John W. Simpson-Porco, *Senior Member, IEEE*, and Gilbert Bergna-Diaz, *Member, IEEE*

***Abstract*—Reactive power sharing and voltage containment for inverter-based resources (IBRs) are two important but related objectives in inverter-based grids. In this paper, we propose a distributed control technique to achieve these objectives simultaneously. Our controller consists of two components: a purely local nonlinear integral controller that adjusts the IBR voltage setpoint, and a distributed primal-dual optimizer that coordinates reactive power sharing among the IBRs using neighbor-to-neighbor communication. The controller prioritizes the voltage containment objective over reactive power sharing *at all times*; except for the IBRs with saturated voltages, it provides reactive power sharing among all IBRs. Considering the voltage saturation and the coupling between voltage and angle dynamics, a formal closed-loop stability analysis based on singular perturbation theory is provided, which provides practical tuning guidance for the overall control system. To validate the effectiveness of the proposed controller for different case studies, we apply it to a low-voltage microgrid, the modified CIGRE medium-voltage network benchmark, and the IEEE 33 bus radial distribution system, all simulated in the MATLAB/Simulink environment.**

***Index Terms*—Distributed optimization, inverter-based resources, reactive power sharing, voltage stability.**

I. Introduction

POWER systems are moving toward the use of more renewable energy, leading to an increasing share of inverter-based resources (IBRs) in power grids. Together with increased uncertainties in power supply and demand, this shift introduces new operational and control challenges, which in turn require new control solutions [1], [2]. Among others, proportional active and reactive power sharing among dispatchable IBRs are two important control objectives. In addition, IBRs that are not dispatchable in terms of active power, such as wind and solar units, can also participate in reactive power sharing [1], [2].

Manuscript received February 27, 2023; revised June 28, 2023; accepted August 01, 2023. Date of publication XXXX XX, 2023; date of current version August 05, 2023. This work was supported by the Department of Electric Energy, NTNU, under Grant 988775100. Paper no. TSG-00285-2023. (Corresponding author: Babak Abdolmaleki.)

B. Abdolmaleki is with the Department of Electric Energy, Norwegian University of Science and Technology, 7491 Trondheim, Norway, and on leave form the Department of Electrical and Computer Engineering, University of Toronto, 10 King's College Road, Toronto, ON, M5S 3G4, Canada (email: babak.abdolmaleki@ntnu.no).

J. W. Simpson-Porco is with the Department of Electrical and Computer Engineering, University of Toronto, 10 King's College Road, Toronto, ON, M5S 3G4, Canada (email: jwsimpson@ece.utoronto.ca).

G. Bergna-Diaz is with the Department of Electric Energy, Norwegian University of Science and Technology, 7491 Trondheim, Norway (email: gilbert.bergna@ntnu.no).

Since frequency is a globally unique variable, it can be used to facilitate active power sharing between IBRs [3]. However, voltage (magnitude) is not globally unique and differs from bus to bus depending on the line impedance values; therefore, it cannot be used to enforce global reactive power sharing [1], [2]. Reactive power flow is most dependent on the bus voltages and their differences. This dependence causes an inherent trade-off between accurate reactive power sharing and individual bus voltage regulation, and motivates a significant amount of research on this topic. Various centralized, decentralized and distributed voltage and reactive power control techniques have been proposed for IBRs. The distributed techniques have attracted considerable attention in power system control, especially for large-scale integration of IBRs [2]. Compared to their centralized counterparts, they rely on information exchange only between neighboring IBRs. In addition, they show better performance and accuracy than decentralized solutions, such as the droop control technique [4]. Therefore, it seems that the real-time distributed techniques can be a viable strategy in many situations [2], [5].

A. Literature Review and Research Gaps

Distributed voltage and reactive power sharing control of IBRs has been studied in many papers. Some papers have focused only on the voltage regulation task and have not considered the reactive power sharing problem. The only objective in these papers is to regulate the voltages of the IBRs to a setpoint. This setpoint may be constant or it may be updated by an external controller. For example, in [6]–[8] and some references therein, assuming that only a few IBRs can directly access the voltage setpoint, a leader-follower consensus algorithm is used for the IBRs to follow this setpoint, which is considered as a virtual leader.

Conversely, in other lines of research, reactive power sharing is considered as the main objective, and voltage control requirements are either neglected or only briefly discussed. For example, in [9]–[12], distributed consensus algorithms are used to ensure proportional reactive power sharing among the IBRs, regardless of the impact of the controllers on the voltages. However, voltage regulation and reactive power sharing are both important, but coupled and conflicting; therefore, they should be considered simultaneously.

Simultaneous reactive power sharing and voltage regulation has also been studied. In [13], a leader-follower consensus-based control is proposed for reactive power sharing and

voltage tracking problems where the voltage setpoint is given by a critical bus voltage regulator. Different versions of this scheme are studied and proposed in [14]–[16]. A somewhat similar controller is proposed in [17] where, unlike in [13], [15], [16], it is assumed that all IBRs can directly access the voltage setpoint. However, these controllers use a single integrator to achieve both objectives, introducing a trade-off factor (gain); therefore, the accuracy of reactive power sharing and voltage regulation depends heavily on the choice of control gains. The existence of a trade-off between the two objectives is also discussed in [16], [17]. In [17], tuning of the control gains is suggested as a possible solution for dealing with this trade-off, while in [16] the issue is left as an open problem.

Another combination of control objectives is precise reactive power sharing and *average* voltage regulation [18]–[24]. In this approach, instead of the individual voltages of the IBRs, their estimated average is controlled to a setpoint. For this purpose, in [18] and some references therein, the leader-follower consensus algorithm is used for average voltage control. Based on the leaderless consensus algorithm, a controller is proposed in [19], where the voltage setpoint of each IBR is corrected by two terms that provide average voltage regulation and accurate reactive power sharing, separately. Similarly, two other approaches are proposed in [20], [21], but the power sharing is achieved by adjusting the droop coefficient [20] or by changing the virtual impedance [21]. To improve the voltage profile and accuracy under input disturbances, some modified controllers are also proposed in [22]–[24].

While the above control schemes can provide average voltage regulation, they can result in large deviations in the individual voltages of the IBRs, violating the limits provided by grid standards, e.g. IEEE 1547 [25]. Therefore, in many applications, voltage containment seems to be a more practical goal [23], [24], [26], [27]. In [23], [26], the problem is formulated as an optimization problem and some controllers based on the primal-dual gradient method are developed. However, these methods require knowledge of the network model and exchange a relatively large amount of information among the IBRs. In [27], along with a consensus-based control for reactive power sharing, a leader-follower voltage containment controller is proposed to force the voltages into a safe band imposed by some minimum and maximum "leader" IBRs. However, the accuracy of reactive power sharing and voltage containment in this method depends on the selection of the *right* leaders; i.e., one must already know which IBRs take voltages closer to the minimum and maximum limits and select them as the leader IBRs. In another attempt to constrain the voltages, [24] introduces a voltage variance estimation and control loop into the scheme of [19]. However, in this method, a "special" IBR is left out of the reactive power sharing task so that the other units can simultaneously achieve accurate reactive power sharing and bounded voltages.

It is worth mentioning the similarity of the problem at hand with the problem of voltage regulation and current/power sharing in dc grids, which has been studied in another line of research, see e.g. [28]–[30]. To the best of our knowledge, these distributed dc grid controllers still do not address the research gaps mentioned in the reviewed literature; for example, the controller in [28] only provides average voltage regulation, the method in [29], similar to the controller in [27], depends on the choice of "leader" converters, and the method in [30] depends on the knowledge of the grid conductance matrix. In addition, inverter-based ac systems have different characteristics from dc systems due to the coupling between voltage and frequency-phase angle dynamics, and therefore require their own dedicated control design and system analysis.

In summary, we have identified the following research gaps. The papers in [6]–[12] have studied *either* regulation of individual IBR voltages *or* reactive power sharing, but not both, while none of the papers in [6]–[22], [28] have considered the operational voltage limits. The accuracy of power sharing and voltage regulation/containment under the proposed controllers in [13]–[17], [23], [24], [26], [27], [29], [30], strongly depends on the choice of control parameters or the selection of special converters. If not properly designed, some of these controllers may not provide steady-state reactive power sharing under voltage limits, even if it is possible. Finally, a rigorous study of the stability and synchronization of the power system considering the coupling between angle and voltage dynamics is lacking in the above works.

B. Contributions

To address the observed research gap, we propose a distributed control scheme for IBRs to achieve voltage containment and reactive power sharing simultaneously. The main contributions of this paper are as follows. ***C1)*** In our proposed method, we use a *distributed primal-dual optimizer* to generate a globally unique setpoint to be tracked by a purely local nonlinear integral controller that regulates the reactive power of the IBR and tunes its voltage setpoint. This architecture allows the *user-defined* voltage constraints to be maintained not only in steady state, but *at all times*, while ensuring that the reactive power demand is shared among the IBRs with *high accuracy*. If the reactive power sharing described above is not possible due to voltage saturation, then our controller excludes only the IBRs with saturated voltages from the reactive power sharing task and allows the other IBRs operating outside the voltage limits to achieve high accuracy reactive power sharing; i.e., the controller prioritizes voltage containment over reactive power sharing, but does not penalize all IBRs. ***C2)*** We analyze the steady state of the system using graph theory and determine its properties. Considering the coupling between voltage and angular dynamics and voltage saturation, we rigorously study the stability of the system using the Lyapunov method (as recommended in [1]). To this end, we consider a timescale separation between the dynamics of the primal-dual optimizer and the voltage-angle dynamics, perform a singular perturbation analysis, and find the stability conditions. We also provide some practical insights into the selection of control parameters based on the IEEE 1547 standard [25] and the stability analysis. ***C3)*** To validate our results, we adapt the proposed scheme to three test systems simulated in the MATLAB/Simulink environment, including the modified CIGRE benchmark medium-voltage distribution network and the modified IEEE 33 bus radial distribution system.

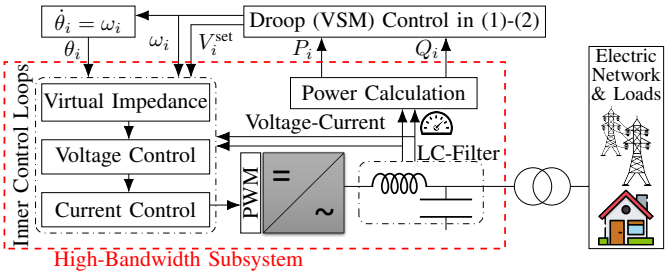

Fig. 1. An inverter-based resource (IBR), governed by the primary control in (1). The high-bandwidth subsystem is denoted by dashed lines. The detailed low-level control structure used in this paper can be found in, e.g., [32].

Our first attempt to address the identified research gap was presented in [31], where we introduced a preliminary version of our control architecture. In this paper, we extend the work in [31] in the following ways. First, we include a leakage term in the local integrator channel to provide anti-wind-up action. Second, we reformulate the selection of the integrator setpoint as an optimization problem. Third, we add a formal stability proof and a parameter selection guideline. Finally, we add several new simulation case studies based on a low-voltage microgrid and the IEEE 33 bus radial distribution system.

The rest of the paper is organized as follows. Section II contains the system modeling and the problem statement. In Section III, we introduce our proposed control scheme. In Section IV, we perform steady state and stability analyses of the control system, where we also provide guidelines for parameter selection. In Section V, we present and discuss the simulation results for several case studies. Finally, Section VI concludes the paper.

II. System Modeling, Power Sharing Definition, and Droop Control Behavior

A. Inverter-based Electric Power Network

Under the hierarchical control policy [1], [2], the innermost control loops of inverters are tasked with controlling the LC filter's inductor current and capacitor voltage by generating proper switching signals (see Fig. 1). While different inner loop designs have been proposed, all are designed to act *very fast*, such that the subsystem denoted by red dashed lines in Fig. 1 has a high bandwidth [2]; virtual impedance control can also be embedded in this subsystem to provide additional decoupling between active and reactive powers and improve system performance [32]. For example, in our simulation case studies in Section V, we use the cascaded control structure described in [32] and references therein. We also assume that the IBRs use the well-known droop control [32] or equivalently virtual synchronous machine (VSM) control technique [4] as their primary controller, which operates slowly compared with the internal control loops.

In a multi-vendor power system, however, the detailed structure and dynamics of the fast internal controllers are not easily accessible. Therefore, for high-level control design and stability studies, it is preferable to use a simplified generic model for each primary-controlled IBR [33], [34]. For the ith IBR we will use the model

$$\dot{\theta}_i = \omega_i = \omega_{\text{nom}} + \Omega_i \tag{1a}$$
$$\tau_\Omega \dot{\Omega}_i = -\Omega_i - m_i^\omega P_i / S_i^{\text{rated}} \tag{1b}$$
$$V_i = V_i^{\text{set}} = V_{\text{nom}} + v_i \tag{2a}$$
$$\tau_v \dot{v}_i = -v_i - m_i^V Q_i / S_i^{\text{rated}} \tag{2b}$$

where θ_i and ω_i are the phase angle and angular frequency of the IBR, V_i and V_i^{set} are the IBR voltage and its setpoint, and ω_{nom} and V_{nom} are the nominal frequency and voltage. The state variables Ω_i and v_i are the frequency and voltage deviations induced by droop (VSM) controllers in (1b) and (2b), respectively. The constants τ_Ω and τ_v are the frequency and voltage time constants, respectively. The constants m_i^ω and m_i^V are the IBR's frequency and voltage droop coefficients, respectively. The apparent power S_i^{rated} is the rated capacity of the IBR while P_i and Q_i are respectively its active and reactive power injections, which are related to $\theta = (\theta_1, \ldots, \theta_n)$ and $V = (V_1, \ldots, V_n)$ through the following power flow equations

$$P_i = f_i^P(\theta, V) = \sum_{j=1}^n V_i V_j \big(G_{ij}\cos(\theta_{ij}) + B_{ij}\sin(\theta_{ij})\big) \tag{3a}$$
$$Q_i = f_i^Q(\theta, V) = \sum_{j=1}^n V_i V_j \big(G_{ij}\sin(\theta_{ij}) - B_{ij}\cos(\theta_{ij})\big) \tag{3b}$$

where $\theta_{ij} = \theta_i - \theta_j$ is the phase difference between IBRs i and j; G_{ij} and B_{ij} are the elements of the network's reduced conductance and susceptance matrices [35, Ch. 6.4].

B. Power Sharing Definition and Review of Droop Control

In this subsection, we define power sharing among IBRs and review the steady-state behavior of droop control. As notation, for any variable x, let $\bar{x}$ denote its steady-state value.

Definition 1. *The microgrid* (1)–(3) *achieves reactive power sharing if* $\bar{Q}_i/S_i^{\text{rated}} = \bar{Q}_j/S_j^{\text{rated}} = \alpha_Q$ *for some* α_Q. *We define active power sharing similarly, using* P *instead of* Q.

According to the droop control in (1b) and (2b) we have

$$\bar{P}_i/S_i^{\text{rated}} = -\bar{\Omega}_i/m_i^\omega, \qquad \bar{Q}_i/S_i^{\text{rated}} = -\bar{v}_i/m_i^V.$$

Since steady-state frequency is global, for every i and j we have $\bar{\Omega}_i = \bar{\Omega}_j$. Thus, following the conventional droop control design criteria [32], by selecting equal frequency droop coefficients for the IBRs, i.e., $m_i^\omega = m_j^\omega$, we have $\bar{P}_i/S_i^{\text{rated}} = \bar{P}_j/S_j^{\text{rated}}$ for every i and j, i.e., the frequency droop controller (1b) enforces proportional active power sharing. However, since $\bar{v}_i = \bar{v}_j$ for every i and j *does not necessarily hold*, selecting $m_i^V = m_j^V$ does not guarantee $\bar{Q}_i/S_i^{\text{rated}} = \bar{Q}_j/S_j^{\text{rated}}$; i.e., the voltage droop controller (2b) cannot enforce reactive power sharing in the same way. In what follows, *in place of the conventional voltage controller* (2), we propose a distributed control scheme to provide reactive power sharing considering the IBRs voltage limits.

III. Proposed Controller

In this section, we introduce our proposed controller. The controller consists of two subsystems that will be introduced

separately: *a)* a nonlinear leaky integral controller for regulating reactive power ratios of the IBRs and maintaining the voltage limits, and *b)* a distributed optimizer for obtaining the optimal setpoint for this integrator.

A. Integral Reactive Power Regulation Under Voltage Limits

Let $V_i^{\min}$ and $V_i^{\max}$ denote minimum and maximum the desired operational voltage limits for IBR i, with average value $V_i^\star = \frac{1}{2}(V_i^{\max} + V_i^{\min})$ and maximum allowable deviation $\Delta_i = \frac{1}{2}(V_i^{\max} - V_i^{\min})$ from that average. *In place of* the conventional voltage controller (2), we propose the nonlinear integral controller

$$V_i = V_i^{\text{set}} = V_i^\star + \Delta_i \tanh(v_i/\Delta_i), \tag{4a}$$

$$\tau_v \dot{v}_i = V_i^\star(\lambda_i - Q_i/S_i^{\text{rated}}) - \beta\Delta_i \tanh(v_i/\Delta_i) - \rho_i(v_i)v_i, \tag{4b}$$

where v_i is the state variable of the integrator (4b) with time constant τ_v, and where $\beta > 0$ is sufficiently small. The variable λ_i is a setpoint for the utilization ratio Q_i/S_i^{rated}, obtained by the optimizer, which will be subsequently described in (8), in the next subsection. The non-negative function $\rho_i(v_i)$ is a nonlinear *leakage* coefficient, defined as

$$\rho_i(v_i) = \begin{cases} |v_i/\Delta_i| - 3 & \text{if } |v_i| > 3\Delta_i \\ 0 & \text{otherwise.} \end{cases} \tag{4c}$$

The main ideas behind the controller (4) are as follows.

- Since $\tanh$ is bounded between -1 and 1, (4a) ensures that $V_i^{\min} < V_i < V_i^{\max}$ at all points in time. In other words, voltage containment is achieved by construction.[1]
- The first term in (4b) provides integral action for the utilization ratio Q_i/S_i^{rated} to track the provided setpoint λ_i. The (small) term $\beta\Delta_i \tanh(v_i/\Delta_i)$ provides damping, which will assist in our subsequent stability analysis.
- The nonlinear gain $\rho_i(v_i)$ in (4c) prevents integrator wind-up when $|v_i| > 3\Delta_i$. The particular choice of the constant 3 is because $|\tanh(\pm 3)| \approx 0.995$ and $\tanh(v_i/\Delta_i)$ does not change significantly for $|v_i| > 3\Delta_i$. In words, roughly speaking, for $|v_i| > 3\Delta_i$ the voltages are saturated with an acceptable accuracy.

B. Distributed Optimization of the Integrator Setpoint λ_i

In (4b), λ_i acts as a setpoint for the utilization ratio Q_i/S_i^{rated}. By Definition 1, reactive power sharing will be achieved if the equilibrium values $\bar{\lambda}_i$ are equal, i.e., if $\bar{\lambda}_i = \bar{\lambda}_j$ for all IBRs i and j. We now discuss the optimal selection $\bar{\lambda}_i$ for this setpoint and introduce a distributed algorithm for its online computation.

Following the above discussion, the optimal setpoint selection $\bar{\lambda}_i$ can be formulated via the optimization problem

$$\min_{\bar{\lambda}_i} \sum\nolimits_{i=1}^n \tfrac{1}{2}\left(\bar{\lambda}_i - \bar{Q}_i/S_i^{\text{rated}}\right)^2 \tag{5a}$$

$$\text{subject to } 0 = \bar{\lambda}_i - \bar{\lambda}_j, \ \forall i, j. \tag{5b}$$

[1]As we will see in the stability analysis, the use of a smooth hyperbolic tangent instead of the standard saturation function, allows us to define a positive-definite Lyapunov function and facilitates the stability analysis under voltage constraints.

We will be seeking a distributed online solution to this optimization problem. To this end, we assume that the IBRs can exchange information over a communication network modeled with an *undirected (bidirectional)* and connected communication graph; see Appendix A for more info on graph theory. With a_{ij} denoting the elements of the adjacency matrix and N_i the set of neighbours of IBR i, the problem (5) is equivalent to

$$\min_{\bar{\lambda}_i} \sum\nolimits_{i=1}^n \tfrac{1}{2}\Big((\bar{\lambda}_i - \frac{\bar{Q}_i}{S_i^{\text{rated}}})^2 + \tfrac{k}{2}\sum\nolimits_{i,j=1}^n a_{ij}(\bar{\lambda}_i - \bar{\lambda}_j)^2\Big), \tag{6a}$$

$$\text{subject to } \bar{z}_i = \sum\nolimits_{j\in N_i} a_{ij}(\bar{\lambda}_i - \bar{\lambda}_j) = 0, \ \forall i, \tag{6b}$$

where $k > 0$. The constraint (6b) implies that $\bar{\lambda}_i = \bar{\lambda}_j$ for all i and j. We define the Lagrangian for the problem (6) as

$$\mathbb{L}(\bar{\lambda}_1, \bar{\zeta}_1, \ldots, \bar{\lambda}_n, \bar{\zeta}_n) = C(\bar{\lambda}_1, \ldots, \bar{\lambda}_n) + \sum\nolimits_{i=1}^n \bar{\zeta}_i \bar{z}_i,$$

where $C(\bar{\lambda}_1, \ldots, \bar{\lambda}_n)$ is the total cost function used in (6a) and $\bar{\zeta}_i$ is the Lagrange multiplier associated with the constraint $\bar{z}_i = 0$. The problem (6) is a quadratic minimization program with linear constraints; hence, Slater's condition holds, and KKT conditions provide necessary and sufficient conditions for optimality [36]. In other words, $\bar{\lambda}_i$, $\bar{\zeta}_i$, and $\bar{z}_i$ are optimal if and only if they satisfy the KKT conditions [36, Ch. 5.5]

$$0 = \bar{\lambda}_i - \bar{Q}_i/S_i^{\text{rated}} + k\sum\nolimits_{j\in N_i} a_{ij}(\bar{\lambda}_i - \bar{\lambda}_j) + \sum\nolimits_{j\in N_i} a_{ij}(\bar{\zeta}_i - \bar{\zeta}_j), \tag{7a}$$

$$0 = \bar{z}_i = \sum\nolimits_{j\in N_i} a_{ij}(\bar{\lambda}_i - \bar{\lambda}_j). \tag{7b}$$

The solution $(\bar{\lambda}_i, \bar{\zeta}_i)$ of (7) can be computed in a distributed manner via the so-called primal-dual dynamics [37]

$$\tau_p \dot{\lambda}_i = Q_i/S_i^{\text{rated}} - \lambda_i + k\sum\nolimits_{j\in N_i} a_{ij}(\lambda_j - \lambda_i) - \sum\nolimits_{j\in N_i} a_{ij}(\zeta_i - \zeta_j), \tag{8a}$$

$$\tau_d \dot{\zeta}_i = \sum\nolimits_{j\in N_i} a_{ij}(\lambda_i - \lambda_j), \tag{8b}$$

where λ_i and ζ_i are now dynamic state variables which are exchanged between neighboring IBRs in real-time. The parameters τ_p and τ_d are the primal and dual dynamics time constants, which for our purposes are tunable gains.

To summarize the overall control architecture: the subsystem (8) generates the setpoint λ_i to be tracked by the regulator (4b), while the regulator (4b) generates the voltage setpoint (4a) that is saturated within limits; (4b) also provides an anti-wind-up function through the leakage term $\rho_i(v_i)v_i$ when necessary. The general scheme of the proposed controller is shown in Fig. 2.

IV. Steady-State, Stability Analysis, and Controller Gain Selection

The closed-loop system consists of the angle dynamics (1), the voltage controller (4) and (8), and the power grid model (3). In this section, we analyze the steady state of the closed-loop system, study its stability, and state its properties. We also give some insights on the selection of the control parameters.

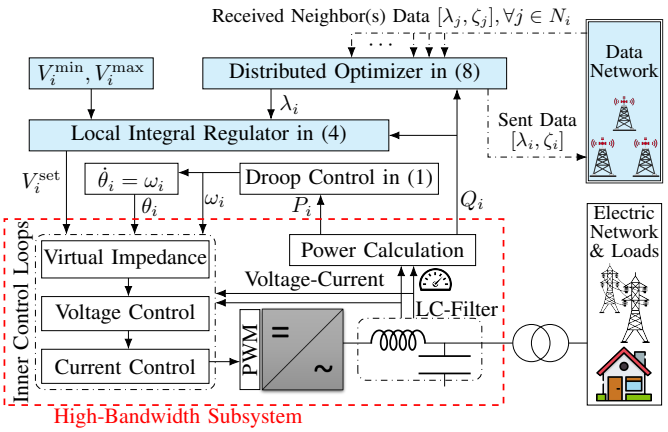

Fig. 2. An IBR under the proposed controller.

A. System Steady State and its Properties

We begin by writing the system dynamics in a compact form. Let $x = \text{col}(x_1, \dots, x_n)$ denote the column vector composed of elements $x_1, \dots, x_n$. We define $m = \text{diag}(m_1^\omega, \dots, m_n^\omega)$, $S = \text{diag}(S_1^{\text{rated}}, \dots, S_n^{\text{rated}})$, and $\rho(v) = \text{diag}(\rho_1(v_1), \dots, \rho_n(v_n))$ as well. With this, we can write the differential equations of (1), (4), and (8) in the compact form

$$\dot{\theta} = \omega = \omega_{\text{nom}} 1_n + \Omega, \tag{9a}$$
$$\tau_\Omega \dot{\Omega} = -\Omega - m S^{-1} P, \tag{9b}$$
$$\tau_v \dot{v} = -\rho(v) v - \beta \Delta \mathbf{tanh}(\Delta^{-1} v) + [V_\star](\lambda - S^{-1} Q), \tag{9c}$$
$$\tau_p \dot{\lambda} = -k \mathcal{L} \lambda - \mathcal{L} \zeta + (S^{-1} Q - \lambda), \tag{9d}$$
$$\tau_d \dot{\zeta} = \mathcal{L} \lambda, \tag{9e}$$

where $\mathcal{L}$ is the Laplacian matrix of the communication graph defined in Appendix A, $1_n = \text{col}(1, \dots, 1) \in \mathbb{R}^n$, $V_\star = \text{col}(V_1^\star, \dots, V_n^\star)$, $\Delta = \text{diag}(\Delta_1, \dots, \Delta_n)$, $\mathbf{tanh}(x) = \text{col}(\tanh(x_1), \dots, \tanh(x_n))$, and $[V_\star] = \text{diag}(V_1^\star, \dots, V_n^\star)$. We can also compactly write the power flow equations (3) and the voltage (4a) as

$$P = f_P(\theta, V) = \text{col}(f_1^P(\theta, V), \dots, f_n^P(\theta, V)), \tag{10a}$$
$$Q = f_Q(\theta, V) = \text{col}(f_1^Q(\theta, V), \dots, f_n^Q(\theta, V)), \tag{10b}$$
$$V = V_\star + \Delta \mathbf{tanh}(\Delta^{-1} v). \tag{10c}$$

Out first result describes equilibrium points of (9)-(10).

Lemma 1 (Steady State)**.** *Consider the system* (9)-(10) *and suppose that the ac power network has a synchronization frequency of* ω_{syn}*. Then any steady state of the system satisfies*

$$\dot{\bar{\theta}} = \omega_{\text{syn}} 1_n = \omega_{\text{nom}} 1_n + \bar{\Omega}, \tag{11a}$$
$$0_n = -\bar{\Omega} - m S^{-1} \bar{P}, \tag{11b}$$
$$0_n = -\rho(\bar{v}) \bar{v} - \beta \Delta \mathbf{tanh}(\Delta^{-1} \bar{v}) + [V_\star](\bar{\lambda} - S^{-1} \bar{Q}), \tag{11c}$$
$$0_n = -k \mathcal{L} \bar{\lambda} - \mathcal{L} \bar{\zeta} + (S^{-1} \bar{Q} - \bar{\lambda}), \tag{11d}$$
$$0_n = \mathcal{L} \bar{\lambda}, \tag{11e}$$

where $0_n = \text{col}(0, \dots, 0) \in \mathbb{R}^n$, $\bar{P} = f_P(\bar{\theta}, \bar{V})$, $\bar{Q} = f_Q(\bar{\theta}, \bar{V})$, *and* $\bar{V} = V_\star + \Delta \mathbf{tanh}(\Delta^{-1} \bar{v})$. *Moreover, if* $m_i^\omega = m_\star$ *for some* $m_\star > 0$ *and all* i*, then*

$$\bar{\Omega} = -m_\star \alpha_P 1_n, \quad \text{where } \alpha_P = (\tfrac{1}{n} 1_n^\top S^{-1} \bar{P}) \in \mathbb{R}, \tag{12a}$$
$$\bar{\lambda} = \alpha_Q 1_n, \quad \text{where } \alpha_Q = (\tfrac{1}{n} 1_n^\top S^{-1} \bar{Q}) \in \mathbb{R}. \tag{12b}$$

Proof. If the ac network has a synchronization frequency of ω_{syn}, then we have $\dot{\bar{\theta}} = \omega_{\text{syn}} 1_n$. Setting this equality together with $\dot{x} = 0_n$ for any other variable x in (9), we can simply derive the steady-state equations (11). Next, we prove (12). According to (11a), we have $\bar{\Omega} = (\omega_{\text{syn}} - \omega_{\text{nom}}) 1_n$. Multiplying this equation by $1_n^\top$, we get $\omega_{\text{syn}} - \omega_{\text{nom}} = \frac{1}{n} 1_n^\top \bar{\Omega}$ and hence $\bar{\Omega} = \frac{1}{n} 1_n 1_n^\top \bar{\Omega}$. On the other hand, from (11b) we have $\bar{\Omega} = -m_\star S^{-1} \bar{P}$, where we used $m_i^\omega = m_\star$ for all i. Using the last two equations, we can derive (12a). By connectivity of the communication graph, every solution of equation (11e) has the form $\bar{\lambda} = \alpha_Q 1_n$ for some $\alpha_Q \in \mathbb{R}$ [38, Ch. 6]. Since the graph is undirected, we also have $1_n^\top \mathcal{L} = 0_n$ [38, Ch. 6]; multiplying (11d) by $1_n^\top$ and using this property we get $1_n^\top \bar{\lambda} = 1_n^\top S^{-1} \bar{Q}$. Setting $\bar{\lambda} = \alpha_Q 1_n$ in this equation, we can finally arrive at (12b). ■

Based on Lemma 1, we can now state several practically important properties of the steady state enforced by our controller.

Proposition 1 (Steady State Properties)**.** *Consider a steady state as given in* (11)*, let* $\mathcal{N}$ *denote the set of all the IBRs, and define the set of voltage-saturated IBRs as*

$$\mathcal{N}_{\text{sat}} = \{ i \in \mathcal{N} \,|\, \rho_i(\bar{v}_i) > 0 \}.$$

If $m_i^\omega = m_\star$ *for all* $i \in \mathcal{N}$*, then the steady state described by Lemma 1 has the following properties:*

1) ***Active Power Sharing and Frequency Regulation:*** *Active power sharing is achieved among all the IBRs and the microgrid's synchronization frequency is* $\omega_{\text{syn}} = \omega_{\text{nom}} - m_\star \frac{1}{n} 1_n^\top S^{-1} \bar{P}$.
2) ***Voltage Containment:*** *The steady-state voltages are all in the safe range, i.e.,* $\bar{V}_i \in (V_i^{\min}, V_i^{\max})$ *for all* $i \in \mathcal{N}$.
3) ***Global Reactive Power Sharing:*** *If* $\mathcal{N}_{\text{sat}} = \emptyset$*, then*

$$|\bar{Q}_i / S_i^{\text{rated}} - \alpha_Q| = \beta |1 - \bar{V}_i / V_i^\star|, \qquad \forall i \in \mathcal{N},$$

i.e., the IBRs achieve reactive power sharing with a small error proportional to β.
4) ***Partial Reactive Power Sharing:*** *If* $\mathcal{N}_{\text{sat}} \neq \emptyset$*, then*

$$|\bar{Q}_i / S_i^{\text{rated}} - \alpha_Q| = \beta |1 - \bar{V}_i / V_i^\star|, \qquad \forall i \notin \mathcal{N}_{\text{sat}},$$
$$|\bar{Q}_i / S_i^{\text{rated}} - \alpha_Q| \leq \beta |1 - \bar{V}_i / V_i^\star| + \rho_i(\bar{v}_i) |\bar{v}_i / V_i^\star|, \ \forall i \in \mathcal{N}_{\text{sat}}.$$

i.e., only the IBRs that are not in $\mathcal{N}_{\text{sat}}$ *achieve the described almost accurate reactive power sharing, and for the IBRs that belong to* $\mathcal{N}_{\text{sat}}$*, the sharing accuracy decreases (deteriorates) as* $\rho_i(\bar{v}_i)$ *increases.*

Proof. According to (12a) and (11b), we have $S^{-1} \bar{P} = \alpha_P 1_n$ and hence $\bar{P}_i / S_i^{\text{rated}} = \bar{P}_j / S_j^{\text{rated}} = \alpha_P$, for every i and j, which according to Definition 1 underlines that active power sharing is achieved among all the IBRs. Inserting (12a) into (11a), we can also write $\omega_{\text{syn}} = \omega_{\text{nom}} - m_\star \frac{1}{n} 1_n^\top S^{-1} \bar{P}$, which

proves property 1. The second property is obvious, as we have $-1 < \tanh(\cdot) < 1$. Next, we prove properties 3 and 4.

Inserting (12b) into (11c), and considering $\mathbf{\Delta tanh}\big(\Delta^{-1}\bar{v}\big) = \bar{V} - V_\star$, we have

$$S^{-1}\bar{Q} = \alpha_Q 1_n - \beta[V_\star]^{-1}(\bar{V}-V_\star) - [V_\star]^{-1}\rho(\bar{v})\bar{v}, \quad (13a)$$
$$\bar{Q}_i/S_i^{\text{rated}} = \alpha_Q - \beta(\bar{V}_i/V_i^\star - 1) - \rho_i(\bar{v}_i)\bar{v}_i/V_i^\star. \quad (13b)$$

Now if $\mathcal{N}_{\text{sat}} = \emptyset$, then for all i we have $\rho_i(\bar{v}_i) = 0$. From (13b), we can therefore write

$$\bar{Q}_i/S_i^{\text{rated}} = \alpha_Q - \beta(\bar{V}_i/V_i^\star - 1), \quad \forall i \in \mathcal{N},$$

which proves property 3. Using the definition of the set $\mathcal{N}_{\text{set}}$, we can similarly write

$$\bar{Q}_i/S_i^{\text{rated}} = \alpha_Q - \beta(\bar{V}_i/V_i^\star - 1), \ \ \forall i \notin \mathcal{N}_{\text{sat}},$$
$$\bar{Q}_i/S_i^{\text{rated}} = \alpha_Q - \beta(\bar{V}_i/V_i^\star - 1) - \rho_i(\bar{v}_i)\bar{v}_i/V_i^\star, \ \ \forall i \in \mathcal{N}_{\text{sat}},$$

which, according to Definition 1, proves property 4. ■

B. Stability Analysis

We want to analyze the stability for the system (9). To this end, we first take some steps to simplify the system dynamics and then analyze stability for the simplified version of (9).

As our controller will maintain voltages within limits around their nominal values, a linearized power flow model is sufficient to describe the network behavior around the operating point [39].

Assumption 1. *Around a nominal operating point, the power flow equations in* (10) *can be approximated by*

$$P = J_\theta^P \theta + J_V^P V + w_P, \quad (14a)$$
$$Q = J_\theta^Q \theta + J_V^Q V + w_Q, \quad (14b)$$

where J_θ^P and J_V^P (resp. J_θ^Q and J_V^Q) are the $n \times n$ Jacobian matrices of $f_P(\theta, V)$ (resp. $f_Q(\theta, V)$) with respect to θ and V at the linearization point, respectively; w_P and w_Q are the corresponding intercepts of the linear functions. The matrices J_θ^P and J_θ^Q each have an eigenvalue at 0 with corresponding right eigenvector 1_n.

We next reduce the order of the system and transform it into relative coordinates, which allows us to leverage *singular perturbation analysis* [40, Ch. 11] and find the stability conditions.

1) ***Model Reduction and Coordinate Transformation****:* As they are tunable control parameters, we can make the following assumption about the time constants τ_Ω, τ_p, τ_d, τ_v in (9).

Assumption 2. *We have $\tau_\Omega, \tau_p \ll \tau_v$ and $\tau_p \ll \tau_d$.*

According to the low-pass filters (9b) and (9d), we have $\Omega = -mS^{-1}P - \tau_\Omega \dot{\Omega}$ and $(I_n + k\mathcal{L})\lambda = -\mathcal{L}\zeta + S^{-1}Q - \tau_p \dot{\lambda}$. Under Assumption 2, the terms $\tau_\Omega \dot{\Omega}$ and $\tau_p \dot{\lambda}$ can be viewed as some negligible parasitic effects; therefore, the system dynamics are mainly governed by (9a), (9c), and (9e). Indeed, one may apply singular perturbation theory to rigorously reduce the order of the system dynamics to the dynamics of θ, v, and ζ (for an example, see [41]); instead, we omit the details and simply eliminate the left-hand sides of equations (9b) and (9d) and consider $\Omega = -mS^{-1}P$ and $(I_n + k\mathcal{L})\lambda = -\mathcal{L}\zeta + S^{-1}Q$. Therefore, considering the linearized power flow equations in Assumption 1, the system (9) reduces to

$$\dot{\theta} = \omega_{\text{nom}} 1_n + \Omega, \quad (15a)$$
$$\tau_v \dot{v} = -\beta V + [V_\star](\lambda - S^{-1}(J_\theta^Q \theta + J_V^Q V + w_Q)) - \rho(v)v + \beta V_\star, \quad (15b)$$
$$\varepsilon \dot{\zeta} = -\tau_v^{-1}\mathcal{L}\mathcal{K}\mathcal{L}\zeta + \tau_v^{-1}\mathcal{L}\mathcal{K}S^{-1}(J_\theta^Q \theta + J_V^Q V + w_Q), \quad (15c)$$
$$\Omega = -mS^{-1}(J_\theta^P \theta + J_V^P V + w_P), \quad (15d)$$
$$\lambda = -\mathcal{K}\mathcal{L}\zeta + \mathcal{K}S^{-1}(J_\theta^Q \theta + J_V^Q V + w_Q), \quad (15e)$$

where $\mathcal{K} = (I_n + k\mathcal{L})^{-1}$ and $\varepsilon = \tau_d/\tau_v$.

We now want to study the stability of the steady state for the system (15) via *singular perturbation analysis*. In particular, the analysis in [40, Theorem 11.3] requires a system evolving on Euclidean space and an exponentially stable fixed point for the fast dynamics. In order to satisfy these requirements, we instead analyze a version of the system (15) in which the system is transformed into relative coordinates. Let us now define the change of coordinates $x_\theta = T\theta = [\theta_{\text{av}}\ r_\theta^\top]^\top$ and $x_\zeta = T\zeta = [\zeta_{\text{av}}\ r_\zeta^\top]^\top$, where θ_{av} and ζ_{av} are respectively the average values of the elements in θ and ζ, the vectors r_θ and r_ζ belong to $\mathbb{R}^{n-1}$, and the transformation matrix $T \in \mathbb{R}^{n \times n}$ is

$$T = \begin{bmatrix} 1/n & 1/n & \dots & 1/n \\ -1 & 1 & & \\ & \ddots & \ddots & \\ & & -1 & 1 \end{bmatrix}, \quad T1_n = \begin{bmatrix} 1 \\ 0 \\ \vdots \\ 0 \end{bmatrix} \in \mathbb{R}^n. \quad (16a)$$

By Assumption 1 and connectivity of the communication graph, the matrices J_θ^P, J_θ^Q, and $\mathcal{L}$ satisfy $J_\theta^P 1_n = J_\theta^Q 1_n = \mathcal{L}1_n = 0_n$ [42] [38, Ch. 6]. Using $T1_n$ in (16a) and these properties, we compute that

$$TJ_\theta^P T^{-1} = T_\theta^P = \begin{bmatrix} 0 & c_P^\top \\ 0_{n-1} & J_{\theta\text{red}}^P \end{bmatrix}, \quad (16b)$$
$$TJ_\theta^Q T^{-1} = T_\theta^Q = \begin{bmatrix} 0 & c_Q^\top \\ 0_{n-1} & J_{\theta\text{red}}^Q \end{bmatrix}, \quad (16c)$$
$$T\mathcal{L}T^{-1} = T_\zeta = \begin{bmatrix} 0 & c_\zeta^\top \\ 0_{n-1} & \mathcal{L}_{\text{red}} \end{bmatrix}, \quad (16d)$$

for $J_{\theta\text{red}}^P, J_{\theta\text{red}}^Q, \mathcal{L}_{\text{red}} \in \mathbb{R}^{(n-1)\times(n-1)}$ and $c_P, c_Q, c_\zeta \in \mathbb{R}^{n-1}$. Let us now use $x_\theta = T\theta$, $x_\zeta = T\zeta$ and write the system dynamics (15) in the new coordinates as

$$\dot{x}_\theta = -TmS^{-1}T^{-1}T_\theta^P x_\theta - TmS^{-1}J_V^P V + \omega_{\text{nom}} T1_n - TmS^{-1}w_P, \quad (17a)$$
$$\tau_v \dot{v} = [V_\star](\mathcal{K} - I_n)S^{-1}T^{-1}T_\theta^Q x_\theta - [V_\star]\mathcal{K}T^{-1}T_\zeta x_\zeta + [V_\star](\mathcal{K} - I_n)S^{-1}J_V^Q V - \beta V - \rho(v)v + \beta V_\star + [V_\star](\mathcal{K} - I_n)S^{-1}w_Q, \quad (17b)$$
$$\varepsilon \dot{x}_\zeta = \tau_v^{-1}T\mathcal{L}\mathcal{K}S^{-1}T^{-1}T_\theta^Q x_\theta + \tau_v^{-1}T\mathcal{L}\mathcal{K}S^{-1}J_V^Q V - \tau_v^{-1}T\mathcal{L}\mathcal{K}T^{-1}T_\zeta x_\zeta + \tau_v^{-1}T\mathcal{L}\mathcal{K}S^{-1}w_Q. \quad (17c)$$

According to (16), the first columns of T_θ^P, T_θ^Q, and T_ζ are all zeros, which means the first elements of x_θ and x_ζ – θ_{av} and ζ_{av} – do not influence the dynamics in (17) at all. Therefore,

(17) is the interconnection of the two cascaded subsystems, given by

$$\dot{r}_\theta = R_\theta r_\theta + R_{\theta V} V + d_\theta, \tag{18a}$$
$$\tau_v \dot{v} = R_{v\theta} r_\theta + (R_{vV} - \beta I_n) V + R_{v\zeta} r_\zeta - \rho(v) v + d_v, \tag{18b}$$
$$\varepsilon \dot{r}_\zeta = R_{\zeta\theta} r_\theta + R_{\zeta V} V + R_\zeta r_\zeta + d_\zeta, \tag{18c}$$
$$\dot{\theta}_{\rm av} = R_\theta^{\rm av} r_\theta + R_{\theta V}^{\rm av} V + d_\theta^{\rm av}, \tag{19a}$$
$$\varepsilon \dot{\zeta}_{\rm av} = 0_n, \tag{19b}$$

where their components are given in Appendix B. It should be noted that to obtain (18)-(19) from the dynamics (17), we have used the properties $r_\theta = I_r x_\theta$, $r_\zeta = I_r x_\zeta$, $\theta_{\rm av} = 1_n^\top T^\top x_\theta$, $\zeta_{\rm av} = 1_n^\top T^\top x_\zeta$, $x_\theta = I_r^\top r_\theta + T 1_n \theta_{\rm av}$, and $x_\zeta = I_r^\top r_\zeta + T 1_n \zeta_{\rm av}$, where $I_r = [0_{n-1}\, I_{n-1}] \in \mathbb{R}^{(n-1)\times n}$.

Clearly, the dynamics of r_θ, r_ζ, and v do not depend on $\theta_{\rm av}$ and $\zeta_{\rm av}$. Therefore, the steady states of (17) and hence (15) are stable, *if and only if* the steady state of (18) is stable. In what follows, we discover this.

*2) **Timescale Separation and Singular Perturbation Analysis**:* We are now interested in studying the stability of the steady state of the system (18) using the idea of timescale separation by considering (18a)-(18b) as the slow dynamics and (18c) as the fast dynamics. The following theorem states the stability conditions under these considerations.

Theorem 1 (Exponential Stability for (18))**.** *Suppose that the linear matrix inequality*

$$\mathcal{P}_\theta \succ 0, \quad \mathcal{D}_v \succ 0, \quad \mathcal{Q} + \mathcal{Q}^\top \prec 0, \tag{20a}$$

in the variables $\mathcal{P}_\theta$ and $\mathcal{D}_v$ has a solution, where $\mathcal{P}_\theta$ is symmetric, $\mathcal{D}_v$ is diagonal, and $\mathcal{Q}$ is

$$\mathcal{Q} = \begin{bmatrix} \mathcal{P}_\theta R_\theta & \mathcal{P}_\theta R_{\theta V} \\ \mathcal{D}_v R_{v\theta}^{\rm new} & \mathcal{D}_v (R_{vV}^{\rm new} - \beta I_n) \end{bmatrix}, \tag{20b}$$

$$\textit{where} \quad \begin{cases} R_{v\theta}^{\rm new} = R_{v\theta} - R_{v\zeta} R_\zeta^{-1} R_{\zeta\theta} \\ R_{vV}^{\rm new} = R_{vV} - R_{v\zeta} R_\zeta^{-1} R_{\zeta V}. \end{cases} \tag{20c}$$

Then, there exists $\varepsilon^\star > 0$ such that for all $\tau_d < \varepsilon^\star \tau_v$ the steady state of the system (18) *is exponentially stable.*

Proof. We consider $\varepsilon = \tau_d/\tau_v$ small and (18c) as the fast dynamics; therefore, the velocity $\dot{r}_\zeta \propto (1/\varepsilon)$ can be large when ε is small and r_ζ in (18c) may rapidly converge to a root of $R_{\zeta\theta} r_\theta + R_{\zeta V} V + R_\zeta r_\zeta + d_\zeta = 0_n$. In other words, the subsystem (18c) may quickly achieve a *quasi-steady state*, where $r_\zeta \approx -R_\zeta^{-1}(R_{\zeta\theta} r_\theta + R_{\zeta V} V + d_\zeta)$. We now define the error between the actual r_ζ and this quasi-steady state as $y = r_\zeta + R_\zeta^{-1}(R_{\zeta\theta} r_\theta + R_{\zeta V} V + d_\zeta)$. We can therefore write (18) as the *singular perturbation problem* below [40, Ch. 11].

$$\dot{r}_\theta = R_\theta r_\theta + R_{\theta V} V + d_\theta, \tag{21a}$$
$$\tau_v \dot{v} = R_{v\theta}^{\rm new} r_\theta + (R_{vV}^{\rm new} - \beta I_n) V + R_{v\zeta} y - \rho(v) v + d_v^{\rm new}, \tag{21b}$$
$$\varepsilon \dot{y} = R_\zeta y + \varepsilon R_\zeta^{-1}(R_{\zeta\theta} \dot{r}_\theta + R_{\zeta V} (\partial V/\partial v) \dot{v}), \tag{21c}$$
$$V = V_\star + \Delta \mathbf{tanh}(\Delta^{-1} v), \tag{21d}$$

where $R_{v\theta}^{\rm new}$ and $R_{vV}^{\rm new}$ are given in (20c) and $d_v^{\rm new} = d_v - R_{v\zeta} R_\zeta^{-1} d_\zeta$. We want to examine the stability of the steady state of (21) by examining the reduced system (22a)-(22b) and boundary-layer system (22c), given as

$$\dot{r}_\theta = R_\theta r_\theta + R_{\theta V} V + d_\theta, \tag{22a}$$
$$\tau_v \dot{v} = R_{v\theta}^{\rm new} r_\theta + (R_{vV}^{\rm new} - \beta I_n) V - \rho(v) v + d_v^{\rm new}, \tag{22b}$$
$$\partial y/\partial \mathbf{t} = R_\zeta y, \tag{22c}$$

where $\mathbf{t} = t/\varepsilon$ is a stretched timescale with t the time. From Appendix B, we have $R_\zeta = -I_r \tau_v^{-1} T \mathcal{L} \mathcal{K} \mathcal{L} T^{-1} I_r^\top$. By the connectivity of the communication graph and the definitions of $\mathcal{K}$, I_r, and T, one can establish that the matrix R_ζ is negative-definite; hence, there exists a symmetric matrix $\mathcal{P}_y \succ 0$ such that $\mathcal{P}_y R_\zeta + R_\zeta^\top \mathcal{P}_y \prec 0$. With the matrix $\mathcal{P}_y$ and the matrices $\mathcal{P}_\theta \succ 0$ and $\mathcal{D}_v \succ 0$ in (20a), we now take the following Lyapunov candidates for the slow (22a)-(22b) and fast (22c) dynamics.

$$\mathcal{S}_s(r_\theta, v) = \tfrac{1}{2} \tilde{r}_\theta^\top \mathcal{P}_\theta \tilde{r}_\theta + \tau_v \int_{0_n}^{\tilde{v}} (\tilde{h}(\tau))^\top \mathcal{D}_v d\tau, \tag{23a}$$
$$\mathcal{S}_f(y) = \tfrac{1}{2} \tilde{y}^\top \mathcal{P}_y \tilde{y}, \tag{23b}$$

where $\tilde{r}_\theta = r_\theta - \bar{r}_\theta$, $\tilde{v} = v - \bar{v}$, and $\tilde{y} = y - \bar{y}$ with $\bar{r}_\theta$, $\bar{v}$, and $\bar{y}$ the steady states in (22), and $\tilde{h}(\tau)$ the following function

$$\tilde{h}(\tau) = \Delta \mathbf{tanh}\big(\Delta^{-1}(\bar{v} + \tau)\big) - \Delta \mathbf{tanh}\big(\Delta^{-1}(\bar{v})\big), \tag{24}$$

which is *element-wise strictly increasing* in τ. Time derivatives of $\mathcal{S}_s$ and $\mathcal{S}_f$ are

$$\dot{\mathcal{S}}_s = \tilde{r}_\theta^\top \mathcal{P}_\theta \dot{\tilde{r}}_\theta + (\tilde{h}(\tilde{v}))^\top \mathcal{D}_v \tau_v \dot{\tilde{v}}, \tag{25a}$$
$$\partial \mathcal{S}_f/\partial \mathbf{t} = \tilde{y}^\top \mathcal{P}_y \partial \tilde{y}/\partial \mathbf{t}. \tag{25b}$$

Inserting the dynamics (22) into (25), we have

$$\dot{\mathcal{S}}_s = -(\tilde{h}(\tilde{v}))^\top \mathcal{D}_v \tilde{\delta}(\tilde{v}) + \tilde{\eta}^\top \mathcal{Q} \tilde{\eta}, \tag{26a}$$
$$\partial \mathcal{S}_f/\partial \mathbf{t} = \tilde{y}^\top \mathcal{P}_y R_\zeta \tilde{y}, \tag{26b}$$

where $\tilde{\delta}(\tilde{v}) = \rho(v)(v) - \rho(\bar{v})\bar{v}$, $\tilde{\eta} = \mathrm{col}(\tilde{r}_\theta, \tilde{h}(\tilde{v}))$ and $\mathcal{Q}$ is as given in (20b). The functions $\tilde{\delta}(\tilde{v})$ and $\tilde{h}(\tilde{v})$ are both element-wise increasing with respect to $\tilde{v}$; therefore, we have

$$-(\tilde{h}(\tilde{v}))^\top \mathcal{D}_v \tilde{\delta}(\tilde{v}) \le 0. \tag{27a}$$

If the matrix inequality (20a) holds, we can write

$$\tilde{\eta}^\top \mathcal{Q} \tilde{\eta} \le -\alpha_s \tilde{\eta}^\top \tilde{\eta}, \tag{27b}$$

where $\alpha_s > 0$ is the smallest eigenvalue of $-(\mathcal{Q} + \mathcal{Q}^\top)$. We can also write

$$\tilde{y}^\top \mathcal{P}_y R_\zeta \tilde{y} = \tilde{y}^\top (\mathcal{P}_y R_\zeta + R_\zeta^\top \mathcal{P}_y) \tilde{y} < -\alpha_f \tilde{y}^\top \tilde{y}, \tag{27c}$$

where $\alpha_f > 0$ is the smallest eigenvalue of $-(\mathcal{P}_y R_\zeta + R_\zeta^\top \mathcal{P}_y)$. Using (27a)-(27c), we can now bound the derivatives in (26) as

$$\dot{\mathcal{S}}_s \le -\alpha_s \tilde{\eta}^\top \tilde{\eta}, \qquad \partial \mathcal{S}_f/\partial \mathbf{t} \le -\alpha_f \tilde{y}^\top \tilde{y}, \tag{28}$$

which, together with the fact that $\mathcal{S}_s$ and $\mathcal{S}_f$ are both positive-definite and radially unbounded, show exponential stability of the steady states of the reduced and boundary-layer dynamics. Now, we can say that the singularly perturbed system (21) satisfies all the assumptions of [40, Theorem 11.3]; therefore, there exists $\varepsilon^\star > 0$ such that for all $\varepsilon < \varepsilon^\star$ or equivalently $\tau_d < \varepsilon^\star \tau_v$, the steady state of (21) is exponentially stable. ■

C. Intuition on Parameter Selection

The tunable control parameters in (1), (2), (4), and (8) are m_i^ω, m_i^V, τ_Ω, τ_p, τ_v, τ_d, k, and β. Following the standard droop control design [32], we select the droop coefficients $m_i^V = \Delta_i$ and $m_i^\omega = m_\star = 2\pi\Delta f_{\max}$ for all i, where $\Delta f_{\max}$ is the maximum steady-state frequency deviation. In what follows, we introduce the impacts and limitations of the remaining parameters and propose a selection procedure.

1) (τ_p, τ_Ω): According to Assumption 2, our stability analysis is based on $\tau_\Omega, \tau_p \ll \tau_v$ and $\tau_p \ll \tau_d$; therefore, the smaller τ_Ω and τ_p, the more reliable our stability analysis. We suggest starting the selection procedure by selecting a small time constant for the low-pass filter (8a), e.g., $\tau_p = 0.01s$. One can, however, select a larger τ_p for better filtering, if required. On the other hand, according to (1a), decreasing the frequency time constant τ_Ω increases $|\dot{f}_i| = \frac{1}{2\pi}|\dot{\omega}_i| = \frac{1}{2\pi}|\dot{\Omega}_i|$, known as the *Rate of Change of Frequency* (RoCoF), which should be limited in practice (see, for example, [25, Table 21]). Thus, we suggest selecting $\tau_\Omega = m_i^\omega/(2\pi \mathrm{RoCoF}^\star)$, where $\mathrm{RoCoF}^\star$ is the maximum withstandable initial RoCoF after a step change in P_i from 0 to S_i^{rated} or vice versa.
2) (τ_v, τ_d): Following the discussion in the previous step, to make our stability analysis more reliable we suggest selecting $\tau_d \gg \tau_p$ and $\tau_v \gg \tau_\Omega, \tau_p$, for example, $\tau_d \geq 10\tau_p$ and $\tau_v \geq \max\{10\tau_\Omega, 10\tau_p\}$. On the other hand, from Theorem 1, one should select $\tau_d < \varepsilon^\star \tau_v$. Since the exact value of $\varepsilon^\star$ is not easily available, we select τ_v as large as possible and τ_d as small as possible, for example, we suggest selecting $\tau_v \geq 10\tau_d$. Combining these suggestions, we get $\tau_d \geq 10\tau_p$ and $\tau_v \geq \max\{10\tau_\Omega, 10\tau_d\}$. Here, it should be noted that, in practice, a small τ_d requires fast (low-latency) inter-IBR data transmissions. But, selecting a large τ_d leads to a large τ_v, which in turn causes slower regulation of the IBR voltage and its reactive power. Therefore, while selecting the control parameters, we should consider the practical standards, e.g., IEEE 1547 [25], on this matter. For example, according to [25, Ch. 5.3] the response time for voltage-reactive power control, depending on the mode and application, varies between 1 to 10 seconds. Selecting $\tau_\Omega, \tau_d \in [0.1s, 1s]$ and following the above suggestions, we get $\tau_v \in [1s, 10s]$ which lies in this acceptable range.
3) (k, β): Clearly, β helps solvability of the linear matrix inequality (20a); it increases the eigenvalues of $-(\mathcal{Q}+\mathcal{Q}^\top)$ and hence the convergence rate α_s in (28). But, according to Proposition 1, it degrades the steady-state reactive power sharing. Therefore, we suggest selecting a desired $k > 0$ first[2] and then selecting a small β such that: ***i)*** the linear matrix inequality (20a) has a solution, and ***ii)*** for every IBR i, the value $\beta\Delta_i/V_i^\star$ is an acceptable upper bound of the error $|\bar{Q}_i/S_i^{\mathrm{rated}} - \alpha_Q|$.

[2]We suggest selecting a desired $k_d > 0$ and computing $k = k_d/\sigma_2$, where σ_2 is the second smallest eigenvalue of $\mathcal{L}$, known as algebraic connectivity of the communication graph [38, Ch. 6].

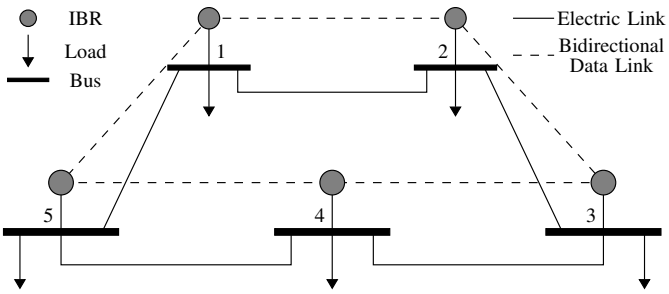

Fig. 3. Test LV microgrid system with specifications given in Table I.

TABLE I
CONTROL AND ELECTRIC SPECIFICATIONS FOR THE LV SYSTEM IN FIG. 3

V_{nom}	$(V_i^{\min}, V_i^{\max})$	S_{Base}	$(\tau_\Omega, m_i^\omega, m_i^V)$
220 [V]	(0.95, 1.05) [p.u.]	100 [kVA]	(0.1, 1.57, 11)
f_{nom}	$\Delta f_{\max}$	(τ_v, τ_d, τ_p)	(β, k_d, k)
50 [Hz]	0.005 [p.u.]	(1, 0.1, 0.01)	(0.01, 10, 7.24)

IBR Capacity + Load Apparent Power and Power Factor					
IBR/Bus #	1	2	3	4	5
S_i^{rated} [p.u.]	1.1	0.6	0.8	0.75	1.3
S_i^{load} [p.u.]	0.9	0.5	0.7	0.65	1
PF_i	0.85	0.9	0.88	0.92	0.87

Bus i to Bus j Interconnection			IBR Output Connection		
(i, j)	r_{ij} [Ω]	x_{ij} [Ω]	IBR #	r_i [Ω]	x_i [Ω]
(1, 2)	0.2	0.3	1	0.03	0.09
(2, 3)	0.19	0.19	2	0.1	0.25
(3, 4)	0.17	0.25	3	0.05	0.15
(4, 5)	0.15	0.22	4	0.08	0.23
(5, 1)	0.22	0.32	5	0.07	0.2

r is resistance and x is reactance.

V. CASE STUDIES AND SIMULATION RESULTS

To verify the effectiveness of the proposed controller, we applied it to a low-voltage 5-bus meshed microgrid system simulated in the MATLAB/Simscape Electrical software environment. The nominal voltage and frequency of the grid are 220 V (RMS) and 50 Hz, respectively. As shown in Fig. 3, the microgrid consists of five local loads powered by five IBRs. Each IBR feeds its respective main bus/load via an output connector. Table I shows the electrical and control specifications of the system. In our simulations, we have adapted the average model of the inverters and internal control loops from [32]. Furthermore, we assume that the IBRs communicate with each other through the network shown by the dashed lines in Fig. 3, where the communication weights for the neighboring IBRs are $a_{ij} = 1$ (cf. Appendix A).

A. Case Study 1: Activation and Load Change

We assume that the droop controllers in (1b) and (2b) control the system before activating the proposed controller. According to Fig. 4(a)-(b), we can see that the voltages deviate from the nominal value, and the IBRs do not share the reactive power proportionally. After activation of the controller at $t = 10s$, the IBRs start changing their voltages so that their reactive power ratios become equal and, at the same time, their voltages maintain within limits $(0.95, 1.05)$ [p.u.]. These results are in line with properties 2 and 3 in Proposition 1.

At $t = 25s$, the load at bus number 5 decreases by 80%, which means to keep the proportional sharing, the 5th IBR

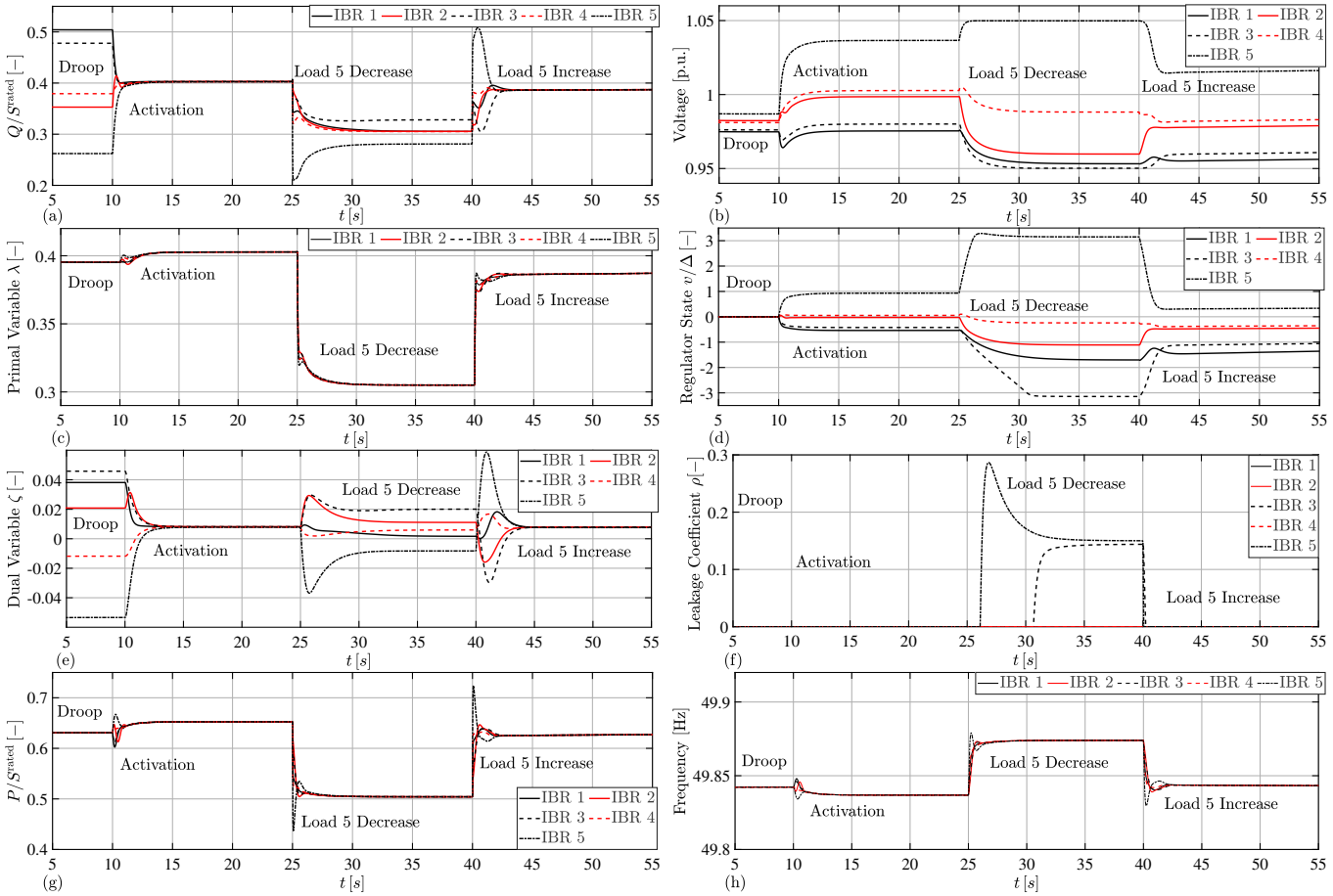

Fig. 4. Simulation results for Case Study 1; (a) reactive power ratios Q_i/S_i^{rated}, (b) voltages V_i, (c) primal variables λ_i, (d) normalized integrator states v_i/Δ_i, (e) dual variables ζ_i, (f) leakage coefficients $\rho_i(v_i)$, (g) active power ratios P_i/S_i^{rated}, and frequencies $f_i = \frac{1}{2}\omega_i/\pi$.

must feed the other loads instead of the lost 80% local load. Therefore, in a collaborative effort to reach an agreement on a new equal power ratio, this IBR increases its voltage, and the other ones reduce their voltages until the IBRs 1, 2, and 4 reach an agreement on Q_i/S_i^{rated}. However, the 3rd and 5th IBRs fail to join this agreement because their voltages are already saturated at the minimum and maximum limits, respectively. However, they have come close to the point of agreement and stayed there. We can observe their effort in reaching a consensus with the other IBRs in Fig. 4(d) and Fig. 4(f). After $t = 25s$, the 5th IBR keeps integrating and increasing v_5/Δ_5 to increase its voltage to the maximum. However, as the voltage is saturated using the $\tanh$ function, the voltage does not change much. Therefore, at $t \approx 26s$, when $v_5 > 3\Delta_5$, the leakage coefficient ρ_5 takes a positive value to prevent the integrator wind-up. Meanwhile, the 3rd IBR also keeps integrating but decreasing h_3/Δ_3, until its voltage gets saturated at $t \approx 34s$ and ρ_3 also takes a positive value. These results are in line with properties 2 and 4 in Proposition 1. After restoring the lost load at $t = 40s$, the IBRs re-achieve proportional reactive power sharing, and their leakage coefficients are all restored to zero. Fig. 4(c) and Fig. 4(e) show the primal-dual variables; we can see that thanks to the dual variables, the primal variable always converges to the average of the reactive power ratios (see (12b)), no matter if the voltages are saturated or not. Therefore, they are treated as a globally-common variable like frequency (see Fig. 6(h)) and used as a reliable reference for the reactive power ratios of the IBRs. We can also see the active and frequency responses in Fig 4(g)-(h), reflecting the impacts of the voltage-reactive power controller on the frequency-active power dynamics.

B. Case Study 2: Eigenvalue Analysis

In this case study we show the effect of different parameters on the eigenvalues of the linearized version of the system (9)-(10). To do this, we increase each parameter in its respective range given in Fig. 5(a)-(f). The parameters are swept 1000 times with equal steps in the given range. According to Fig. 5(a), increasing τ_Ω moves some of the oscillatory eigenvalues toward the imaginary axis and decreases their associated damping values. From Fig. 5(b), we can see that increasing the parameter τ_p does not significantly affect the critical eigenvalues, and increasing it only slows down the system dynamics. According to Fig. 5(c), a small controller time constant τ_v creates some oscillatory eigenvalues, while increasing it only slows down the dynamics and leads to small but highly damped eigenvalues. It should also be noted that a small τ_v can lead to poor performance or even instability

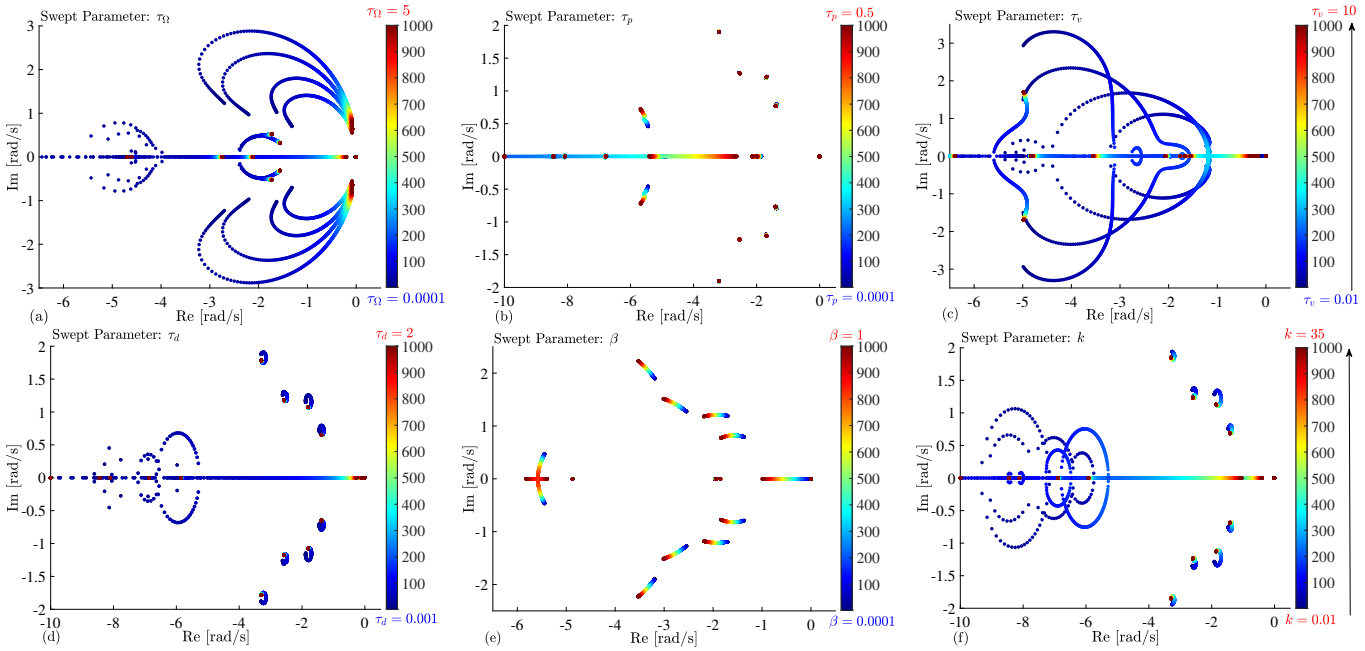

Fig. 5. Results for Case Study 2 (eigenvalue analysis); trace of the eigenvalues for increase of (a) τ_Ω, (b) τ_p, (c) τ_v, (d) τ_d, (e) β, and (f) k.

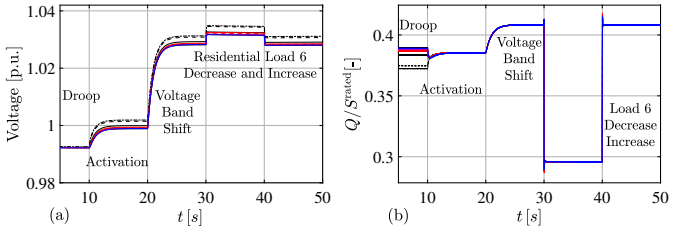

Fig. 6. Simulation results for Case Study 3 (CIGRE network); (a) voltages and (b) reactive power ratios Q_i/S_i^{rated}.

because the voltage dynamics will interfere with the inverter internal control loops, which are not modeled here and are assumed to act very quickly. From Fig. 5(d), decreasing the dual dynamics time constant τ_d shifts the eigenvalues to the left and speeds up the synchronization of the primal variables. According to Fig. 5(e), the parameter β increases the damping of all eigenvalues and improves the transient performance of the system. However, according to Section IV-C, it causes steady-state inaccuracy of reactive power sharing. Finally, as Fig. 5(f) shows, the proportional gain k improves the transient performance by damping the oscillations.

C. Case Study 3: CIGRE Benchmark and Voltage Level Shift

We also applied our controller to a system based on the Subnetwork 1 of the European medium-voltage (20-kV,50-Hz) distribution network benchmark, provided by CIGRE Task Force C6.04.02 [43]. Except for the following modifications, all the specifications of the test system are the same as the original network. Based on the Task Force recommendation, the simulated microgrid is an isolated 9-bus subnetwork of the CIGRE system composed of buses number 3 to 11. All the distributed generators at each bus are lumped into one single dispatchable IBR governed by the proposed controller. To meet the maximum load demand in the islanded microgrid the rated power of the IBRs are all increased by 50%. The control gains are similar to the previous case study, but the voltage limits are $(0.98, 1.02)$ [p.u.]. The simulation results are shown in Fig. 5. At $t = 10s$, the controller is activated and the voltages and reactive powers are controlled properly. At $t = 20s$, we shift the voltage level by setting the new limits $(1.01, 1.05)$ [p.u.]. At $t = 30s$ and $t = 40s$, we disconnect and connect back the residential loads at buses 6 and 8. The results highlight that under the proposed method, we can shift the voltage level in a controlled way while keeping reactive power sharing at different voltage levels.

D. Case Study 4: Unbalanced Load Condition

In this case study, we apply the proposed controller to the microgrid in Fig. 3 with a severe unbalanced load condition. To do this, we replace each balanced load with a single-phase load with the same nominal active and reactive power requirements. The single-phase loads on buses 1 to 5 are placed on phases *ab*, *ab*, *ac*, *bc*, and *bc*, respectively. Using the Fortescue transformation [44], [45], we derive the positive and negative sequence (PS and NS) components of the voltage and current signals $(V_i^+, V_i^-, I_i^+, I_i^-)$, and from these, the PS and NS active and reactive powers of the IBRs $(P_i^+, P_i^-, Q_i^+, Q_i^-)$. We use the PS active and reactive powers in the system equations (1b), (2b), (4b), and (8a). The generated voltage and frequency setpoints are fed to the standard internal voltage and current loops of the IBRs without incorporating additional controllers to compensate for the NS voltage and current components. The simulation results are given in Fig. 7.

According to Fig. 7(a)-(b), the controller can keep the positive sequence (PS) voltages V_i^+ within the limits, while

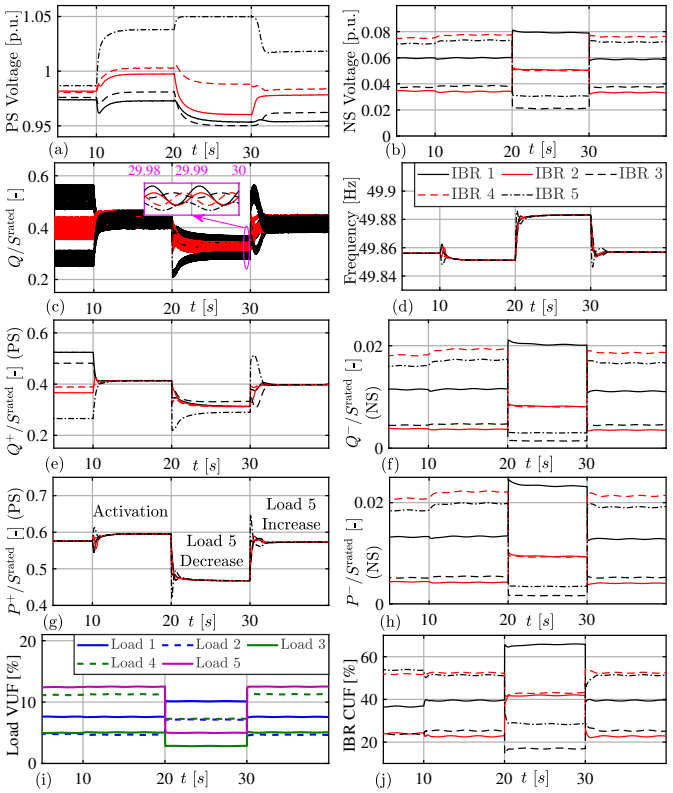

Fig. 7. Simulation results for Case Study 4 (unbalanced load condition); (a) positive sequence voltages V_i^+, (b) negative sequence voltages V_i^-, (c) instantaneous reactive power ratios Q_i/S_i^{rated}, (d) frequencies $f_i = \frac{1}{2}\omega_i/\pi$, (e) positive sequence reactive power ratios Q_i^+/S_i^{rated}, (f) negative sequence reactive power ratios Q_i^-/S_i^{rated}, (g) positive sequence active power ratios P_i^+/S_i^{rated}, (h) negative sequence active power ratios P_i^-/S_i^{rated}, (i) load voltage unbalance factors (VUFs) $100V_l^-/V_l^+$, and (j) IBR current unbalance factors (CUFs) $100I_i^-/I_i^+$.

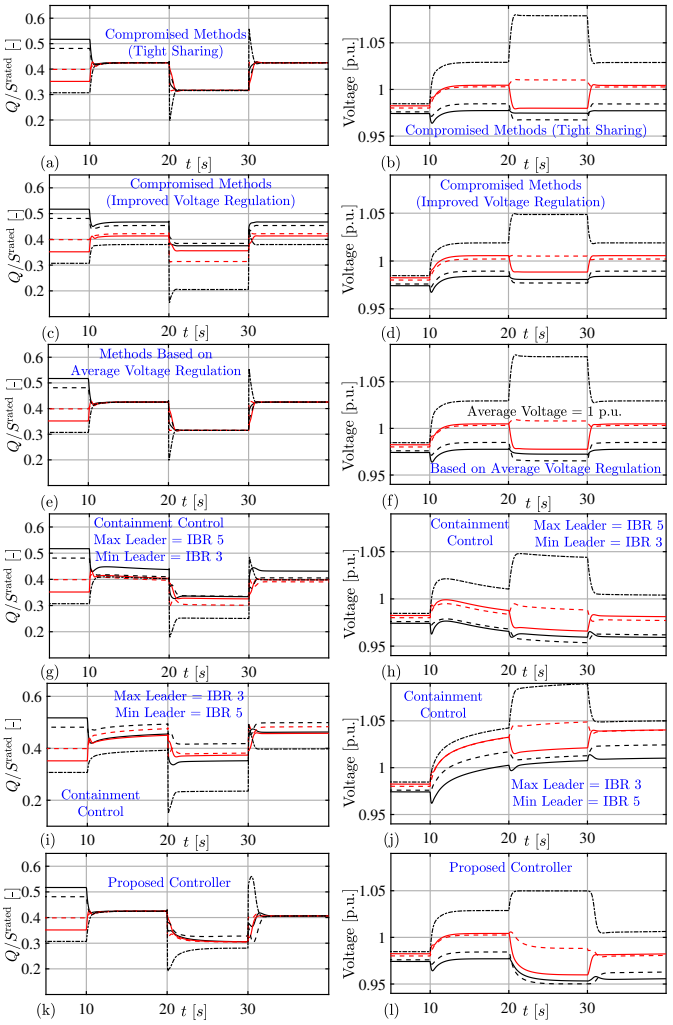

Fig. 8. Simulation results for Case Study 5 (comparison with existing methods). The figures in the first and second rows, i.e. (a)-(d), show the results under the compromised voltage and reactive power sharing controllers in [13]–[17] for different voltage control gains. The figures in the third row (e)-(f) show the results under the controllers that aim to regulate the average of the IBR voltages, for example, the controllers in [18]–[24], [28]. The fourth and fifth rows show the results under the containment control algorithm in [27], [29] for different choices of maximum and minimum IBR "leaders". The last row shows the results under the proposed controller.

the negative sequence (NS) voltage components take non-zero values. In Fig. 7(c)-(d), we can observe that despite the appearance of the 2nd harmonic (100 Hz) oscillations in the instantaneous reactive power responses, the controller can keep the sharing of the average instantaneous reactive power and frequency synchronization almost the same as for the balanced load condition. This can be better understood from Fig. 7(e)-(h), where it is shown that the sharing of PS reactive and active powers (Q_i^+ and P_i^+) is achieved while the IBRs generate non-zero NS power. Fig. 7(i)-(j) show the voltage and current unbalance factors VUF and CUF (see e.g. [44] for the definition). It can be seen that under the proposed controller, the IBRs can still maintain a good level of voltage balancing compared to current balancing while providing PS reactive power sharing and voltage containment. These factors can be improved by incorporating additional internal control loops (see, e.g., [45, Fig. 3]) or possibly using similar distributed controllers to provide NS reactive power sharing, which is beyond the scope of this paper. This, along with the use of accurate power flow models for unbalanced networks (see, for example, [39]), is an interesting topic for future research.

E. Case Study 5: Comparison With the Existing Methods

In this case study, we compare the steady-state voltage and reactive power responses of the system under the proposed controller with those under the existing methods. For fairness, we simulate the system under different methods but with a similar activation and load change scenario and show the results in Fig. 8. At $t = 10s$, the controllers are activated and load number 5 is decreased and increased at $t = 20s$ and $t = 30s$, respectively. According to Fig. 8(a)-(d), the accuracy of reactive power sharing and voltage containment under the compromised controllers in [13]–[17] is highly dependent on the selected trade-off factor (control gain). The controller in Fig. 8(a)-(b) prioritizes sharing over voltage regulation. Therefore, in the heavy load condition, i.e., for $t \in [20s, 30s]$, some IBR voltages (IBR 5) exceed the limits. The controller in Fig. 8(c)-(d) gives more weight to the voltage regulation,

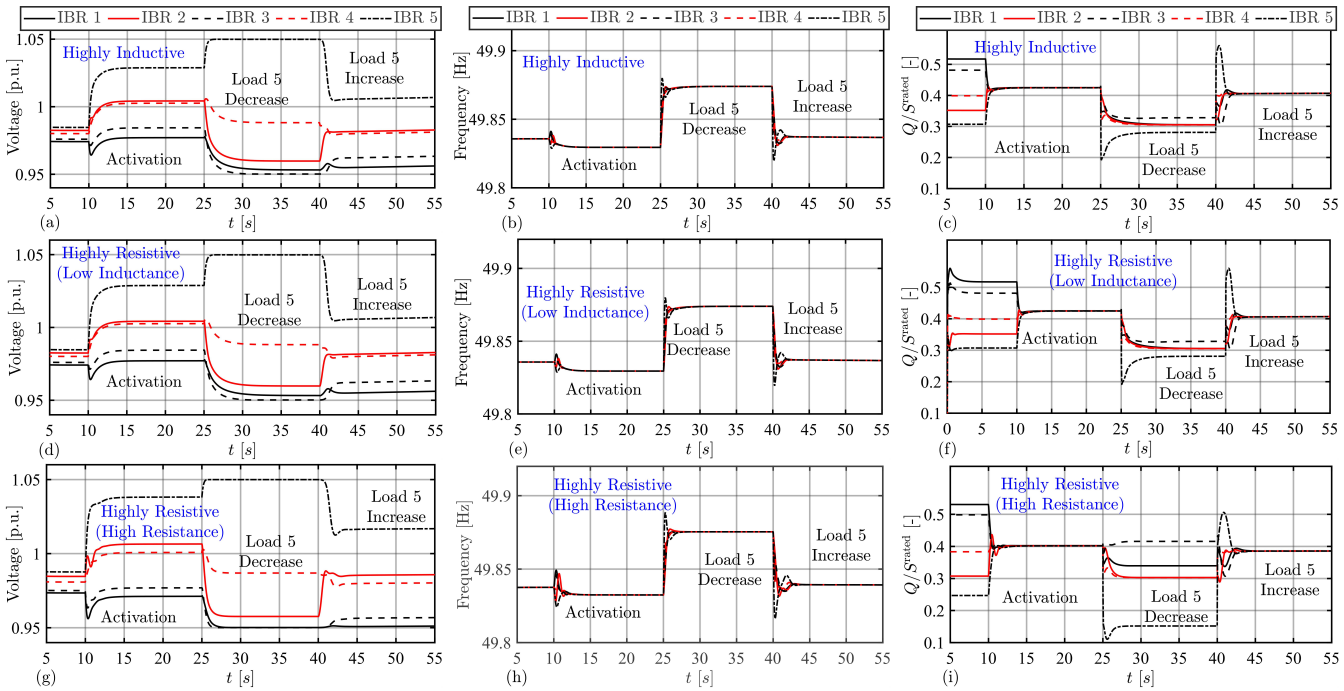

Fig. 9. Simulation results for Case Study 6 (resistive vs. inductive lines); (a) voltages V_i, (b) frequencies $f_i = \frac{1}{2}\omega_i/\pi$, and (c) reactive power ratios Q_i/S_i^{rated}. The figures in the first row (a)-(c) show the results for high line x/r ratios, where the line reactances are 10 times the original values in Table I. The figures in the second row (d)-(f) are the results for low x/r ratios, where the line reactances are 10% of the values in Table I. The figures in the second row (g)-(i) are the results for low x/r ratios, where the line reactances are 20% and the line resistances are twice the values in Table I.

so that in the light load condition, that is at $t \in [10s, 20s]$, there is poor power sharing.

Fig. 8(e)-(f) show the results for the methods that aim to regulate the average of the IBR voltages, e.g. [18]–[24], [28]. It can be seen that these methods can lead to large deviations in the individual voltages of the IBRs (IBR 5) under heavy load conditions, thus violating the limits. Fig. 8 (g)-(j) show the results under the containment control algorithm proposed in [27], [29], for different choices of the maximum and minimum IBR "leaders" (see [27], [29] for details). We can see that even for a correct choice of the maximum and minimum IBR leaders, i.e., IBRs 5 and 3, this method cannot provide accurate power sharing under light load condition. Moreover, according to Fig. 8(i)-(j), with wrong choice of "leader IBRs", the steady-state responses are even worse. Finally, the figures in the last row, Fig. 8(k)-(l), show the results under the proposed solution. It can be seen that the voltages are always within limits, in the light load condition the reactive power sharing is achieved among the IBRs, and in the heavy load condition the sharing is achieved with high accuracy.

F. Case Study 6: Highly Inductive vs. Highly Resistive Lines

To investigate the effect of the line x/r (reactance/resistance) ratio on the system, we apply the controller to the system in Fig. 3 but with different line resistance and reactance values. The simulation results are shown in Fig. 9, where the details of the x/r changes are given in the caption. According to these results, the proposed method can be successfully applied to both resistive and inductive networks. Moreover, we can observe that the performance of the system, both in transient and steady state, depends most strongly on the line resistances rather than on the x/r ratios.

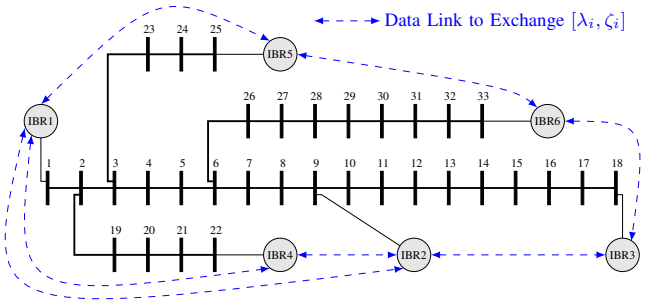

Fig. 10. Modified IEEE 33 bus radial distribution system. The original electrical parameters can be found in [46], while the modifications are explained in Section V-G.

G. Case Study 7: Plug-and-Play and Scalability With IEEE 33 Bus Radial Distribution System

To study the applicability of the proposal to larger systems with radial topology, we simulated the IEEE 33 bus radial distribution system [46], where we performed different events such as frequent IBR and load connection/disconnection. The network topology, given in Fig. 10, is the same as the original one. We place 6 IBRs on buses 1, 9, 18, 22, 25 and 33 numbered as shown in Fig. 10. To meet the maximum load requirement and without using shunt capacitors, we consider IBRs 1 through 6 to have capacities of 3, 1, 0.75, 0.75, 0.75, and 1 MVA, respectively. To emphasize the effectiveness of

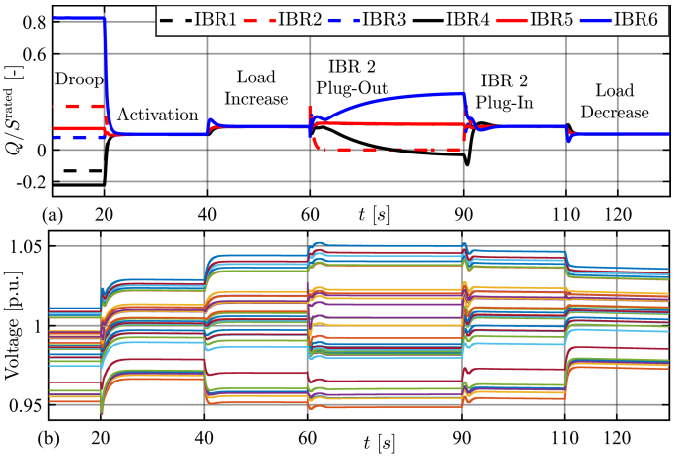

Fig. 11. Simulation results for Case Study 7 (IEEE 33 bus system); (a) bus voltages for all the 33 buses, (b) the IBRs' reactive power ratios Q_i/S_i^{rated}.

our proposal, we also increase all line resistances by 70%. All other control parameters are the same as in the previous test case and are chosen according to the guidelines given in Section IV-C. To apply the proposed control solution, we assume that the IBRs exchange the primal-dual states over the distributed neighbor-to-neighbor communication network shown in Fig. 10. The simulation results are shown in Fig. 11.

Before $t = 20s$, the IBRs are controlled by droop control and the load is at the lowest daily demand as given in [46]. We can see that the reactive power is not shared proportionally and that some of the bus voltages are prone to violate the lower limit if the load demand increases. After activating the proposed controller at $t = 20s$, the reactive power demand is shared proportionally and the bus voltages are shifted away from the limits. At $t = 40s$, the load demand increases to the maximum daily demand given in [46], and the controller can still maintain the voltage limits and distribute the reactive power proportionally among the IBRs. At $t = 60s$, the 2nd IBR is disconnected from the grid. To compensate for the lost reactive power support from IBR 2 and to maintain the voltage limits, IBRs 1, 3, and 5 jointly agree on a new reactive power ratio, while IBRs 4 and 6 increase and decrease their reactive power injections, respectively. After reconnecting IBR 2 at $t = 90s$, it immediately participates in the sharing task. At $t = 110s$, the load demand decreases and so do the voltage differences.

VI. Conclusion

Voltage regulation and reactive power sharing in power systems are two highly coupled control objectives. This coupling is because reactive power flow between two nodes depends more strongly on their voltage differences than the absolute values of the voltages. We proposed a nonlinear controller based on a hyperbolic tangent function and a distributed primal-dual optimizer. The controller provides the IBRs with acceptable reactive power sharing while keeping their voltages within some user-defined limits. We also found stability conditions for the system considering the voltage-angle couplings, under timescale separation between the voltage and optimizer dynamics. The numerical simulations, followed by a proposed parameter selection guideline, indicated a promising performance from the proposed method in controlling the voltage level of the network and achieving reactive power sharing among the IBRs.

Appendix A
Communication Network Model and Graph Theory

An inter-IBR data network can be modeled by an undirected graph where the IBRs and communication links are considered its nodes and edges, respectively. Let $\mathcal{G} = (\mathcal{N}, \mathcal{E}, \mathcal{A})$ be a graph with $\mathcal{N} = \{1, ..., n\}$, $\mathcal{E} \subseteq \mathcal{N} \times \mathcal{N}$, and $\mathcal{A} = [a_{ij}] \in \mathbb{R}^{n\times n}$ being its node set, edge set, and adjacency matrix, respectively. If the nodes i and j directly exchange data, they are neighbors, meaning that $(i, j) \in \mathcal{E}$ and $(j, i) \in \mathcal{E}$, and $a_{ij} = a_{ji} = 0$; otherwise, $a_{ij} = a_{ji} = 0$. Let $N_i = \{j \mid (j, i) \in \mathcal{E}\}$ and $d_i = \sum_{j\in N_i} a_{ij}$ be the neighbor set and in-degree associated with node i, respectively. Laplacian matrix of $\mathcal{G}$ is defined as $\mathcal{L} = \mathcal{D} - \mathcal{A}$, where $\mathcal{D} = \text{diag}\{d_i\}$. A walk (or path) from node i to node j is an ordered sequence of nodes such that any pair of consecutive nodes in the sequence is an edge of the graph. A graph is connected if there exists a walk between any two nodes [38].

Appendix B
Components of the Reduced Dynamics in (18)

With $I_r = [0_{n-1}\, I_{n-1}] \in \mathbb{R}^{(n-1)\times n}$, one can obtain the components of the system (18) as

$$\begin{cases} R_\theta = -I_r T m S^{-1} J_\theta^P T^{-1} I_r^\top, \qquad R_{\theta V} = -I_r T m S^{-1} J_V^P, \\ R_{v\theta} = [V_\star](\mathcal{K} - I_n) S^{-1} J_\theta^Q T^{-1} I_r^\top, \\ R_{vV} = [V_\star](\mathcal{K} - I_n) S^{-1} J_V^Q, \qquad R_{v\zeta} = -[V_\star]\mathcal{K}\mathcal{L} T^{-1} I_r^\top, \\ R_{\zeta\theta} = I_r \tau_v^{-1} T \mathcal{L}\mathcal{K} S^{-1} J_\theta^Q T^{-1} I_r^\top, \\ R_{\zeta V} = I_r \tau_v^{-1} T \mathcal{L}\mathcal{K} S^{-1} J_V^Q, \quad R_\zeta = -I_r \tau_v^{-1} T \mathcal{L}\mathcal{K}\mathcal{L} T^{-1} I_r^\top, \end{cases}$$

$$\begin{cases} R_\theta^{\text{av}} = -1_n^\top T^\top T m S^{-1} J_\theta^P T^{-1} I_r^\top \\ R_{\theta V}^{\text{av}} = -1_n^\top T^\top T m S^{-1} J_V^P \\ d_\theta = I_r \omega_{\text{nom}} T 1_n - I_r T m S^{-1} w_P \\ d_v = \beta V_\star + [V_\star](\mathcal{K} - I_n) S^{-1} w_Q \\ d_\zeta = I_r \tau_v^{-1} T \mathcal{L}\mathcal{K} S^{-1} w_Q \\ d_\theta^{\text{av}} = 1_n^\top T^\top \omega_{\text{nom}} T 1_n - 1_n^\top T^\top T m S^{-1} w_P. \end{cases}$$

References

[1] M. Farrokhabadi *et al.*, "Microgrid stability definitions, analysis, and examples," *IEEE Trans. Power Syst.*, vol. 35, no. 1, pp. 13–29, Jan. 2020.
[2] Y. Khayat *et al.*, "On the secondary control architectures of ac microgrids: An overview," *IEEE Trans. Power Electron.*, vol. 35, no. 6, pp. 6482–6500, Jun. 2020.
[3] B. Abdolmaleki *et al.*, "An instantaneous event-triggered hz–watt control for microgrids," *IEEE Trans. Power Syst.*, vol. 34, no. 5, pp. 3616–3625, Sept. 2019.
[4] S. D'Arco and J. A. Suul, "Equivalence of virtual synchronous machines and frequency-droops for converter-based microgrids," *IEEE Trans. Smart Grid*, vol. 5, no. 1, pp. 394–395, Jan. 2014.
[5] D. K. Molzahn *et al.*, "A survey of distributed optimization and control algorithms for electric power systems," *IEEE Trans. Smart Grid*, vol. 8, no. 6, pp. 2941–2962, Nov. 2017.

[6] B. Abdolmaleki *et al.*, "A zeno-free event-triggered secondary control for ac microgrids," *IEEE Trans. Smart Grid*, vol. 11, no. 3, pp. 1905–1916, May 2020.

[7] A. Afshari *et al.*, "Robust cooperative control of isolated ac microgrids subject to unreliable communications: A low-gain feedback approach," *IEEE Syst. J.*, vol. 16, no. 1, pp. 55–66, Mar. 2022.

[8] G. Zhao, L. Jin, and Y. Wang, "Distributed event-triggered secondary control for islanded microgrids with disturbances: A hybrid systems approach," *IEEE Trans. Power Syst.*, to be published.

[9] J. Schiffer *et al.*, "Voltage stability and reactive power sharing in inverter-based microgrids with consensus-based distributed voltage control," *IEEE Trans. Control Syst. Technol.*, vol. 24, no. 1, pp. 96–109, Jan. 2016.

[10] X. Li *et al.*, "Resilience for communication faults in reactive power sharing of microgrids," *IEEE Trans. Smart Grid*, vol. 12, no. 4, pp. 2788–2799, Jul. 2021.

[11] Y. C. C. Wong *et al.*, "Consensus virtual output impedance control based on the novel droop equivalent impedance concept for a multi-bus radial microgrid," *IEEE Trans. Energy Convers.*, vol. 35, no. 2, pp. 1078–1087, Jun. 2020.

[12] J. Zhou, M.-J. Tsai, and P.-T. Cheng, "Consensus-based cooperative droop control for accurate reactive power sharing in islanded ac microgrid," *IEEE J. Emerg. Sel. Top. Power Electron.*, vol. 8, no. 2, pp. 1108–1116, Jun. 2020.

[13] A. Bidram, A. Davoudi, and F. L. Lewis, "A multiobjective distributed control framework for islanded ac microgrids," *IEEE Trans. Ind. Informat.*, vol. 10, no. 3, pp. 1785–1798, Aug. 2014.

[14] S. I. Habibi *et al.*, "Multiagent-based nonlinear generalized minimum variance control for islanded ac microgrids," *IEEE Trans. Power Syst.*, to be published.

[15] J. Choi, S. I. Habibi, and A. Bidram, "Distributed finite-time event-triggered frequency and voltage control of ac microgrids," *IEEE Trans. Power Syst.*, vol. 37, no. 3, pp. 1979–1994, May 2022.

[16] P. Ge *et al.*, "Resilient secondary voltage control of islanded microgrids: An eskbf-based distributed fast terminal sliding mode control approach," *IEEE Trans. Power Syst.*, vol. 36, no. 2, pp. 1059–1070, Mar. 2021.

[17] J. W. Simpson-Porco *et al.*, "Secondary frequency and voltage control of islanded microgrids via distributed averaging," *IEEE Trans. Ind. Electron.*, vol. 62, no. 11, pp. 7025–7038, Nov. 2015.

[18] Y. Wang *et al.*, "Cyber-physical design and implementation of distributed event-triggered secondary control in islanded microgrids," *IEEE Trans. Ind. Appl.*, vol. 55, no. 6, pp. 5631–5642, Nov./Dec. 2019.

[19] V. Nasirian *et al.*, "Droop-free distributed control for ac microgrids," *IEEE Trans. Power Electron.*, vol. 31, no. 2, pp. 1600–1617, Feb. 2016.

[20] Q. Shafiee *et al.*, "A multi-functional fully distributed control framework for ac microgrids," *IEEE Trans. Smart Grid*, vol. 9, no. 4, pp. 3247–3258, Jul. 2018.

[21] J. Zhou *et al.*, "Consensus-based distributed control for accurate reactive, harmonic, and imbalance power sharing in microgrids," *IEEE Trans. Smart Grid*, vol. 9, no. 4, pp. 2453–2467, Jul. 2018.

[22] M. Shi *et al.*, "Pi-consensus based distributed control of ac microgrids," *IEEE Trans. Power Syst.*, vol. 35, no. 3, pp. 2268–2278, May 2020.

[23] S. M. Mohiuddin and J. Qi, "Optimal distributed control of ac microgrids with coordinated voltage regulation and reactive power sharing," *IEEE Trans. Smart Grid*, vol. 13, no. 3, pp. 1789–1800, May 2022.

[24] S. M. Mohiuddin and J. Qi, "Droop-free distributed control for ac microgrids with precisely regulated voltage variance and admissible voltage profile guarantees," *IEEE Trans. Smart Grid*, vol. 11, no. 3, pp. 1956–1967, May 2020.

[25] *IEEE Standard for Interconnection and Interoperability of Distributed Energy Resources with Associated Electric Power Systems Interfaces*, IEEE Std. 1547-2018, Rev. 2, 2018, (Revision of IEEE Std 1547-2003).

[26] L. Ortmann *et al.*, "Fully distributed peer-to-peer optimal voltage control with minimal model requirements," *Electric Power Systems Research*, vol. 189, p. 106717, 2020.

[27] R. Han *et al.*, "Containment and consensus-based distributed coordination control to achieve bounded voltage and precise reactive power sharing in islanded ac microgrids," *IEEE Trans. Ind. Appl.*, vol. 53, no. 6, pp. 5187–5199, Nov./Dec. 2017.

[28] B. Abdolmaleki and G. Bergna-Diaz, "Distributed control and optimization of dc microgrids: A port-hamiltonian approach," *IEEE Access*, vol. 10, pp. 64 222–64 233, 2022.

[29] R. Han *et al.*, "Compromised controller design for current sharing and voltage regulation in dc microgrid," *IEEE Trans. Power Electron.*, vol. 34, no. 8, pp. 8045–8061, Aug. 2019.

[30] Z. Fan, B. Fan, and W. Liu, "Distributed control of dc microgrids for optimal coordination of conventional and renewable generators," *IEEE Trans. Smart Grid*, vol. 12, no. 6, pp. 4607–4615, Nov. 2021.

[31] B. Abdolmaleki and G. Bergna-Diaz, "Voltage containment and reactive power-sharing in microgrids: Centralized and distributed approaches," in *2022 International Conference on Smart Energy Systems and Technologies (SEST)*, Eindhoven, Netherlands, 2022, pp. 1–6.

[32] X. Wu, C. Shen, and R. Iravani, "Feasible range and optimal value of the virtual impedance for droop-based control of microgrids," *IEEE Trans. Smart Grid*, vol. 8, no. 3, pp. 1242–1251, May 2017.

[33] M. Naderi *et al.*, "Low-frequency small-signal modeling of interconnected ac microgrids," *IEEE Trans. Power Syst.*, vol. 36, no. 4, pp. 2786–2797, Jul. 2021.

[34] B. Abdolmaleki and Q. Shafiee, "Online kron reduction for economical frequency control of microgrids," *IEEE Trans. Ind. Electron.*, vol. 67, no. 10, pp. 8461–8471, Oct. 2020.

[35] P. Kundur, J. B. Neal, and G. L. Mark, *Power System Stability and Control*. New York, NY, USA: McGraw-Hill, 1994.

[36] S. Boyd and L. Vandenberghe, *Convex Optimization*. USA: Cambridge University Press, 2004.

[37] A. Cherukuri, E. Mallada, and J. Cortés, "Asymptotic convergence of constrained primal–dual dynamics," *Systems & Control Letters*, vol. 87, pp. 10–15, Jan. 2016.

[38] F. Bullo, *Lectures on Network Systems*, 1st ed. Kindle Direct Publishing, 2022. [Online]. Available: http://motion.me.ucsb.edu/book-lns

[39] A. Bernstein *et al.*, "Load flow in multiphase distribution networks: Existence, uniqueness, non-singularity and linear models," *IEEE Trans. Power Syst.*, vol. 33, no. 6, pp. 5832–5843, Nov. 2018.

[40] H. K. Khalil, *Nonlinear Systems*, 3rd ed. Englewood Cliffs, NJ, USA: Prentice Hall, 2002.

[41] F. Dörfler and F. Bullo, "Synchronization and transient stability in power networks and nonuniform kuramoto oscillators," *SIAM Journal on Control and Optimization*, vol. 50, no. 3, pp. 1616–1642, 2012.

[42] J. W. Simpson-Porco and F. Bullo, "Distributed monitoring of voltage collapse sensitivity indices," *IEEE Trans. Smart Grid*, vol. 7, no. 4, pp. 1979–1988, Jul. 2016.

[43] K. Strunz *et al.*, "Benchmark systems for network integration of renewable and distributed energy resources," Task Force C6.04, CIGRE, Paris, France, Technical Brochure 575, 2014.

[44] M. Yao, I. A. Hiskens, and J. L. Mathieu, "Mitigating voltage unbalance using distributed solar photovoltaic inverters," *IEEE Trans. Power Syst.*, vol. 36, no. 3, pp. 2642–2651, May 2021.

[45] S. Bera *et al.*, "Hierarchical control for voltage unbalance mitigation considering load management in stand-alone microgrid," *IEEE Trans. Smart Grid*, to be published.

[46] S. H. Dolatabadi *et al.*, "An enhanced ieee 33 bus benchmark test system for distribution system studies," *IEEE Trans. Power Syst.*, vol. 36, no. 3, pp. 2565–2572, May 2021.

Babak Abdolmaleki (Graduate Student Member) received the B.Sc. and M.Sc. degrees in electrical engineering from Shiraz University, Shiraz, Iran, in 2014 and 2017, respectively. He is currently a Ph.D. Candidate at the Department of Electric Energy, Norwegian University of Science and Technology (NTNU), Trondheim, Norway. From September 2017 to March 2020, he was a Research Associate with the Smart/Micro Grid Research Center (SMGRC) at the University of Kurdistan, Sanandaj, Iran. From September 2022 to February 2023, he was a Visiting PhD Student at the Systems Control Group at the University of Toronto, Toronto, ON, Canada. His research interests include numerical simulation, feedback control, automation, and optimization of dynamical systems applied to power electronics and power systems. He is an active member of IEEE and CIGRE.

John W. Simpson-Porco (Senior Member) received the B.Sc. degree in engineering physics from Queen's University, Kingston, ON, Canada, in 2010, and the Ph.D. degree in mechanical engineering from the University of California at Santa Barbara, Santa Barbara, CA, USA, in 2015. He is currently an Assistant Professor of Electrical and Computer Engineering with the University of Toronto, Toronto, ON, Canada. He was previously an Assistant Professor with the University of Waterloo, Waterloo, ON, Canada and a Visiting Scientist with the Automatic Control Laboratory, ETH Zürich, Zürich, Switzerland. His research interests include feedback control theory and applications of control in modernized power grids. Prof. Simpson-Porco was the recipient of the Automatica Paper Prize, the Center for Control, Dynamical Systems and Computation Best Thesis Award, and the IEEE PES Technical Committee Working Group Recognition Award for Outstanding Technical Report. He is currently an Associate Editor for the IEEE Transactions on Smart Grid.

Gilbert Bergna-Diaz (Member) received the degree in electrical power engineering from the Universidad Simón Bolívar, Caracas, Venezuela, in 2008, the research master's degree in electrical energy from the École Supérieure dÉlectricité (Supélec), Paris, France, in 2010, and the joint Ph.D. degree in electric power engineering from the École Centrale Supélec, Paris, and the Norwegian University of Science and Technology (NTNU), Trondheim, Norway, in 2015. In 2014, he joined SINTEF Energy Research as a Research Scientist, where he was involved in modelling, analysis, and control of HVdc transmission systems. In 2016, he joined the Department of Electric Power Engineering, NTNU, as a Post-Doctoral Research Fellow, where he was involved in energy-based modeling and nonlinear control of multiterminal HVdc grids. Since 2019, he has been an Associate Professor with the Department of Electric Energy (former Electric Power Engineering) at NTNU.